Multi-wavelength Observations of 3C 273 in 1993-1995

C. von Montigny[1,23,24], H. Aller[2], M. Aller[2], F. Bruhweiler[3], W. Collmar[4], T.J.-L. Courvoisier[8], P. G. Edwards[19], C. E. Fichtel[1], A. Fruscione[5], G. Ghisellini[21], R. C. Hartman[1], W. N. Johnson[20], M. Kafatos[6], T. Kii[19], D. A. Kniffen[7], G. G. Lichti[4], F. Makino[19], K. Mannheim[22], A.P. Marscher[15], B. McBreen[16], I. McHardy[17], J. E. Pesce[9], M. Pohl[4], E. Ramos[6], W. Reich[10], E.I. Robson[11], K. Sasaki[19], H. Teräsranta[12], M. Tornikoski[12], C. M. Urry[9], E. Valtaoja[12,13], S. Wagner[14], T. Weekes[18]

[1] NASA/Goddard Space Flight Center, Code 661, Greenbelt, MD 20771

[2] Astronomy Department, University of Michigan, Dennison Building, Ann Arbor, MI, 48109-1090

[3] Dept. of Physics, Catholic University of America, Washington, D.C. 20064

[4] Max-Planck-Institut für extraterrestrische Physik, 85740 Garching, Germany

[5] Harvard-Smithsonian Center for Astrophysics, 60 Garden Street, Cambridge, MA 02138

[6] Center for Earth Observations and Space Research, CSI, George Mason University, Fairfax, VA 22030

[7] Hampden-Sydney College, P.O. Box 862, Hampden-Sydney, VA 23943

[8] INTEGRAL Science Data Center, 16 Chemin d'Ecogia, CH-1290 Sauverny, Switzerland

[9] Space Telescope Science Institute, 3700 San Martin Drive, Baltimore MD 21218

[10] Max-Planck Institut für Radioastronomie, Bonn, Germany

[11] Joint Astronomy Centre, 660 N. Aohoku Place, Hilo HI 96720

[12] Metsähovi Radio Research Station, FIN-02540 Kylmala, Finland

[13] Tuorla Observatory, University of Turku, SF-21500, Piikkiö, Finland

[14] Landessternwarte Heidelberg-Königstuhl, D-69117 Heidelberg, Germany

[15] Department of Astronomy, Boston University, 725 Commonwealth Ave., Boston MA 02215

[16] Physics Department, Univ. College, Belfield, Dublin 4, Ireland

[17] Department of Physics, University of Southampton, Southampton S09 5NH, UK

---

[24]present address: Landessternwarte Heidelberg-Königstuhl, D-69117 Heidelberg, Germany

[18] Whipple Observatory, Harvard-Smithsonian Center for Astrophysics, Box 97, Amado AZ 85645

[19] Inst. of Space & Astronaut. Science, Yoshinodai 3-1-1, Sagamihara, Kanagawa 229, Japan

[20] E.O. Hulburt Center for Space Research, Code 7650, Naval Research Laboratory, Washington, DC 20375

[21] Osservatorio di Brera-Merate, V. Bianchi, 46, Merate, Italy

[22] Universitäts-Sternwarte, Geismarlandstrasse 11, D-37803 Göttingen, Germany

[23] NAS/NRC Resident Research Associate, NASA/GSFC

Subject headings: gamma rays: observations — galaxies: active — quasars: individual: 3C 273

ABSTRACT

We present the results of the multi-wavelength campaigns on 3C 273 in 1993-1995. During the observations in late 1993 this quasar showed an increase of its flux for energies $\geq$ 100 MeV from about $2.1 \cdot 10^{-7}$ photons cm^{-2}s^{-1} to approximately $5.6 \cdot 10^{-7}$ photons cm^{-2}s^{-1} during a radio outburst at 14.5, 22 and 37 GHz. However, no one-to-one correlation of the γ-ray radiation with any frequency could be found. The photon spectral index of the high energy spectrum changed from $\Gamma_\gamma = (3.20 \pm 0.54)$ to $\Gamma_\gamma = (2.20 \pm 0.22)$ in the sense that the spectrum flattened when the γ-ray flux increased. Fits of the three most prominent models (synchrotron self-Comptonization, external inverse Comptonization and the proton initiated cascade model) for the explanation of the high γ-ray emission of active galactic nuclei were performed to the multi-wavelength spectrum of 3C 273 . All three models are able to represent the basic features of the multi-wavelength spectrum. Although there are some differences the data are still not decisive enough to discriminate between the models.

1. Introduction

The identification of 54 EGRET γ-ray sources with radio-loud active galactic nuclei (AGN) (Thompson et al. 1995, 1996) has drawn the attention of the astronomical community to these very interesting extragalactic objects. The observations have shown

that for all AGN detected by EGRET the energy output in the high energy regime is at least as high as, and during active periods can be as much as 10-30 times, that in the optical regime. An extensive summary of the results from phases 1 and 2 (1991 May 16 to 1993 August 17) of the observations of these AGNs with EGRET and their implications has been given by von Montigny et al. (1995).

3C 273 shows all the characteristics which are typical for high luminosity quasars: a flat radio spectrum of the core, strong and rapid variability in the optical and other energy ranges (Courvoisier et al. 1988, Courvoisier et al. 1990), variable polarization, a radio jet with superluminal motion. Additionally, it shows an optical and X-ray jet and a very prominent UV excess, the so-called "big blue bump". Although 3C 273 is not a high polarization quasar (HPQ) — for which the standard definition is that the *optical* polarization exceeds 3% at least once — it is an interesting borderline case between high and low polarization quasars (LPQs). Sometimes it is dubbed a 'miniblazar' since it shows polarization flares similar to the true HPQs, but only up to the 1% level, and almost hidden by the non-polarized flux variations (Impey et al. 1989, Valtaoja et al. 1990, Valtaoja et al. 1991).

It is one of the best studied quasars and has been detected and observed in every energy band from radio to γ-rays. It was first detected as a very bright radio double source (Schmidt 1963). Component A of the double source was identified with the optical quasar (Schmidt 1963, Conway et al. 1982) and has a very flat radio spectrum ($S \sim \nu^{\alpha_r}$) with a spectral index α_r = -0.01 ± 0.07 between 2.7 and 5 GHz (Kühr et al. 1981). Component B is associated with an optical jet and its radio spectral index is much steeper: $\alpha_r \approx$ -0.7. Its apparent magnitude in the optical is m_v = 12.5 mag. The optical jet is one-sided and faint.

3C 273 was first identified as an X-ray source by Bowyer et al. (1970). Its luminosity in the 2 - 10 keV band is $\sim 10^{46}$ erg/s and the X-ray spectral index in this energy band varies in the range -0.25 $\leq \alpha_x \leq$ -0.5 (Courvoisier et al. 1987). An X-ray feature coinciding with one of the enhancements in the optical jet was discovered by the EINSTEIN-HRI (Harris & Stern 1987). Two detections of a high energy γ-ray source in the Virgo region were reported with the COS-B satellite in 1976 and 1978. This γ-ray source was identified with 3C 273 because of the positional coincidence (Swanenburg et al. 1978, Bignami et al. 1981).

During the all-sky survey of the Compton observatory in Phase 1 (1991 May to 1992 November), 3C 273 was detected by all four instruments aboard the observatory (BATSE: Paciesas et al. 1994; OSSE: McNaron-Brown et al. 1994; COMPTEL: Hermsen et al. 1993, Williams et al. 1995; EGRET: von Montigny et al. 1993). The main result from Phase 1 is the presence of another maximum in the energy output in the 1-10 MeV range

of the electromagnetic spectrum which is about as high as the maximum of the UV-Bump (Lichti et al. 1994, 1995).

Because 3C 273 is such a well-studied, bright object from radio through X-rays it seems to be well suited for detailed studies in order to learn more about the physical processes taking place in quasars. Intensive studies of the variability have already been performed in order to look for correlations between different energy bands (Courvoisier et al. 1987, Robson et al. 1993). These studies found correlations between the infra-red (1.25μm(J); 1.65μm(H); 2.2μm(K); 3.8μm(L$'$); 800μm) and shortest radio wavelengths (1.1 mm and 3.3 mm). However, these correlations were not seen for every flare but only in some (Robson et al. 1993).

Since those studies did not include the high energy γ-ray range, an international campaign was organized to observe 3C 273 simultaneously at all wavelengths from radio through MeV and TeV γ-ray energies during Phase 3 (1993 August 17 to 1994 October 3) and Cycle 4 (1994 October 4 to 1995 October 3) of the Compton Observatory mission, in the hope that it would be possible to discriminate between the various models which have been developed in order to explain the γ-ray emission from blazars: (i) the synchrotron self-Compton (SSC) model (e.g. Maraschi, Ghisellini, & Celotti 1992, Bloom & Marscher 1992,1993); (ii) the inverse Compton process on external photons (EC-models) which could be either photons from the accretion disk (Dermer, Schlickeiser, & Mastichiadis 1992) or reprocessed photons from the broad-line region (Sikora, Begelman, & Rees 1994, Dondi & Ghisellini 1995), or (iii) synchrotron emission from ultra-relativistic electrons and positrons produced in a proton-induced cascade (Mannheim & Biermann 1992, Mannheim 1993a). We are aware that there are even more models. But we can not consider all these models here since it would go beyond the scope of this paper which is mainly to present the data from the multiwavelength campaign. Hence, we concentrate only on the three basic models. For an overview of models see e.g. von Montigny et al. (1995) and references therein.

In this paper we describe observations of 3C 273 with EGRET during Phases 2, 3 and Cycle 4 of the Compton observatory mission (§2) as well as simultaneous or quasi-simultaneous observations across the entire electromagnetic spectrum during Phase 3 (§3). The results are given in §4. In §5 we present a discussion of the results.

2. EGRET observations and analysis

A detailed description of the EGRET instrument is given by Kanbach et al. (1988). The instrument calibration, both before and after launch, is presented by Thompson et al.

(1993).

The analysis of the EGRET data (Fichtel et al. 1994) used counts and exposure maps for photon energies for different energy intervals as well as the diffuse γ-ray background predicted by the standard EGRET analysis software from HI and CO distributions (Bertsch et al. 1993, Hunter et al. 1996). The maps containing all events with energies $\geq$ 100 MeV were used for the detection and determination of the position of the source in order to avoid the rather broad point spread function ($\geq 5°$) below 100 MeV. For the determination of the spectrum of the source, the maps containing 10 standard energy intervals were used.

This analysis used a maximum likelihood method which simultaneously gives the best fit of the diffuse background to the data (Mattox et al. 1996). Prominent EGRET sources other than 3C 273 in the viewing period under consideration were added iteratively to the diffuse background model. Throughout the analysis a photon spectrum power law index of Γ_γ=2.0 was assumed for the spectra of the sources which is a typical spectral index for the strong EGRET blazars (von Montigny et al. 1995, Chiang et al. 1995). The formal significance of a source detection in standard deviations is determined from the square root of the likelihood test statistic TS (Eadie et al. 1971, Mattox et al. 1996) which is given by two times the natural logarithm of the ratio of the maximum likelihood values for the alternative and the null-hypothesis.

2.1. Time variability

Table 1 lists the observations, the fluxes and significances from the EGRET observations in phases 1, 2, 3 and cycle 4. When the source has TS < 9 (corresponding to a formal significance of < 3σ) it is regarded as not detected and 2σ upper limits are given.

After the initial detection of 3C 273 by EGRET in 1991 June (viewing period (VP) 3) in phase 1 (von Montigny et al. 1993) its flux (always for energies $\geq$ 100 MeV) had decreased in strength during later observations in 1991 October (VP 11) and in 1992 December through 1993 January (VP 204 through 206) in phase 1 and 2 (von Montigny et al. 1993, Sreekumar et al. 1996); only upper limits could be derived (see also Table 1 and Fig. 3, bottom panel). Then in phase 3 during 1993 October to 1993 December (VP's 304 - 308.6) and 1993 mid-December to 1994 January (VP's 311 - 313) the flux of 3C 273 increased from about $2.1 \cdot 10^{-7}$photons cm^{-2}s^{-1} to approximately $5.6 \cdot 10^{-7}$photons cm^{-2}s^{-1} between 1993 October 19 and 1993 December 1 (VP's 304 through 308.6). This is an increase by about a factor of 3 within 43 days (Fig. 3, bottom panel) and it is the only time so far that EGRET has seen 3C 273 to be at about the same flux level ($6.0 \cdot 10^{-7}$photons cm^{-2}s^{-1}) as

during the COS-B observations (Swanenburg et al. 1978, Hermsen et al. 1981). Fourteen days later, and again in Cycle 4 (1994 November 21 through 1995 January 3) it returned to a quiet state.

2.2. Spectrum

We derived spectra from each viewing period and sums of viewing periods in which 3C 273 was detected with a significance greater than 3σ. In order to determine the spectra the estimated number of source counts in ten observed energy intervals was determined by a likelihood analysis (Mattox et al. 1996).

The simplest spectral model that adequately fit the data was a power law of the form

$$dN/dE = N_o(E/E_o)^{-\Gamma_\gamma}$$

where E_o is the energy scale factor chosen so that the statistical errors in the power law index, Γ_γ, and the overall normalization, N_o, are uncorrelated.

The values of the parameters N_o, Γ_γ and E_o are given in Table 2 for the different observations. The gamma-ray photon spectral index was found to vary from viewing period to viewing period from $\Gamma_\gamma = (3.20\pm0.54)$ to $\Gamma_\gamma = (2.20\pm0.22)$. The errors are determined from $\Delta\chi^2 = 1$ (see Dingus et al. 1996).

Figure 1 compares the spectra from 3C 273 during VP 305 and VP308.6 with each other. These are the observations where 3C 273 had the lowest and the highest flux in phase 3, respectively. It can be seen that the increase in flux results from the hardening and pivoting of the spectrum around the low energy end.

There appears to be a correlation between the spectral index and the integral flux above 100 MeV in phase 3 (Fig. 2). The linear correlation coefficient between these two variables is -0.91, and the significance level at which the null hypothesis of zero correlation is disproved is 1.1%. However, if one includes the data from VP 3 and COS-B, the linear correlation coefficient changes to about -0.72, corresponding to a probability that this set of data was drawn from a uniform distribution of about 4.3%. The significance of the correlation is not very high since the errors on both variables are rather large. Since this correlation is not yet compelling we will use the average EGRET spectrum derived from the sum of the viewing periods 304 through 308.6 for the rest of the paper. Nevertheless, there is evidence that the γ-ray spectra harden when the source flux increases. There are indications for this behaviour not only from 3C 273 but also from other γ-ray sources. Mücke et al. (1996a) did a statistical analysis of this relation with all EGRET sources for

which spectra and fluxes were available (e.g. 0528+134, Mukherjee et al. 1996; 1222+216, Sreekumar et al. 1996; 3C 279, Kniffen et al. 1993). They also find that the average source appears to have a harder spectrum at high γ-ray states. The chance probability is of the order of 10^{-5}.

3. Multiwavelength observations

Soon after the discovery of the June 1991 flare in 3C 279 and the realization that most of the γ-ray blazars are highly time variable, it was recognized that simultaneous observations of these sources across the entire electromagnetic spectrum are of crucial importance for the understanding of their emissions. This led to an international campaign to observe 3C 273 simultaneously at as many wavelengths as possible in 1993 and 1994. The following section reports on the results of these observations.

3.1. Radio

Reich et al. (1993) have already described the multifrequency observing method used at the Effelsberg 100-m telescope to monitor variable sources as detected by EGRET. The observations result in quasi-simultaneous flux density measurements at 2.7 GHz, 5 GHz and 10.7 GHz.

Observations at 22 and 37 GHz were made at the Metsähovi Radio Research Station. The observing procedures are described in detail in Teräsranta et al. (1992). The data presented here are weekly mean values.

Observations were also made with the University of Michigan's 26-meter telescope at 4.8, 8.0 and 14.5 GHz. A description of the data reduction is given in Aller et al. (1985). The fluxes are daily averages. Table 3(a-f) lists the radio data used here.

3.2. Millimeter and sub-millimeter

The 3 mm and 1.3 mm (90 GHz and 230 GHz, respectively) observations were made with the Swedish-ESO Submillimetre Telescope (SEST) at the European Southern Observatory site of Cerro La Silla, Chile.

For the 3 mm observations a dual polarisation Schottky receiver in a double sideband mode was used. For the 1.3 mm observations a Schottky receiver and a wide band

acousto-optic spectrometer were used initially, but later a single channel bolometer was used for most of the sessions. The bolometer had a bandwidth of about 50 GHz, centered at 236 GHz. To convert the intensities into flux densities, the measurements were calibrated against planets, with 3C 274 as a secondary calibrator (Tornikoski et al. 1996).

Data were also obtained at wavelengths of 450, 800, 1100, 1300 and 2000 microns using the JCMT at Mauna Kea (Duncan et al. 1990). Tables 4(a-f) summarize the results from the observations in the mm- and sub-mm wavebands.

3.3.   IR and optical

Observations have been carried out in UBVRIJHK with sparse sampling at the Swiss 0.7m telescope on La Silla, the 0.7m telescope in Heidelberg and with UKIRT in Hawaii using standard CCD detectors and a NICMOS 3 array camera. The data are shown in Table 5. Observational procedures and data calibration has been carried out as described in Courvoisier et al. (1987).

3.4.   UV/EUV

3C 273 is observable by IUE only during the time intervals mid-December – mid-February and May – mid-June. There were observations of 3C 273 with IUE on 1993 January 8 (2 SWP respectively 3 LWP spectra coadded) and 1994 June 20 (4 SWP, 4 LWP) as well as from 1995 January 3 to 12 (20 SWP, 21 LWP). The average exposure for SWP spectra was $\sim$ 30 minutes and for LWP spectra $\sim$ 25 minutes.

We have also obtained EUVE coverage of 3C 273 with the EUVE Deep Survey/Spectrometer during the 1994 January 8 to 14 (modified julian dates: 49360 - 49366) time frame for a total of 205,219 s (effective exposure time: 130,093 s). The total photometric flux in the range 67 – 178 Å was $(7.2\pm 0.081)\cdot10^{-2}$ counts/s. For details about the analysis see Ramos et al. (1996).

Table 6 lists the results of these observations. A reddening correction for interstellar absorption of E(B-V) = 0.03 has been applied to the values from the reddening law of Seaton (1979). The errors in fluxes are obtained by also taking into account the calibration error of IUE ($\sim$ 5-10%).

3.5. X-rays

ASCA observed 3C 273 for calibration purposes on five different occasions namely on 1993 December 16, 19, 20, 23 and 27. Assuming a single power law with the Galactic absorption ($N_H = 1.8 \cdot 10^{20}$ H-atoms/cm^2) in the 0.5-10 keV range a spectrum for 3C 273 could be derived from these measurements. Details of the ASCA instrument and its calibration are given in Makishima et al. (1996) and references therein. Table 7 contains the results which were obtained using the 1994 versions of the instrumental response and efficiency functions for the analysis.

3.6. High energy observations

The OSSE instrument is sensitive to γ-rays in the 0.05 – 10 MeV range. It consists of four identical but independently positionable detector systems providing an orientation range of 192°. For details about the instrument and analysis procedures, see e.g. Johnson et al. (1993, 1995). OSSE observed 3C 273 simultaneously with COMPTEL and EGRET only for 7 days from 1993 December 20 to 27 (VP 312). The results from these observations are given in Table 8.

The COMPTEL energy range (0.75 – 30 MeV) overlaps with the OSSE energy range. Detailed descriptions of the instrument can be found in Schönfelder et al. (1993). COMPTEL has also detected 3C 273 and Table 9 gives the fluxes derived by a maximum likelihood method (for its application to COMPTEL data see de Boer et al. 1992). The spectrum obtained is the average over two distinct time periods: 1993 October 19 to December 1 and 1993 December 13 to 1994 January 3 (VP's 304 – 313).

The Whipple Telescope observed 3C 273 during several epochs. The observation closest in time to the EGRET observations is from 1994 March. 3C 273 was not detected during that observation. Therefore, only an upper limit could be provided. For energies $\geq$ 0.3 TeV the flux limit was $< 1.7 \cdot 10^{-11}$ photons cm^{-2}s^{-1} . Assuming an E^{-2} power law this flux value corresponds to a flux density $F_\nu < 1.1 \cdot 10^{-2}$ pJy.

4. Results

4.1. Multifrequency Variability

In the case of 3C 273 it seems that the gamma radiation is possibly related to the slower radio outbursts at 14.5, 22 and 37 GHz. There are two slower outbursts at 22 and 37 GHz, the first peaking around 1991.67 (MJD $\sim$ 48470) and the second around 1993.96 (MJD $\sim$ 49330). The second outburst peaks first at 37 GHz then at 22 GHz and finally at 14.5 GHz. The second outburst does not look as impressive because it is buried within the decline of the very strong first outburst; nevertheless it still represents a major radio burst. All the detections of 3C 273 with EGRET occured during the rising parts or at the maxima of the major, slower radio outbursts. Most of the non-detections were during the declining part of these burst components or during a very early stage of the outburst (Fig. 3, 2nd and 4th panels).

The γ-emission disappeared during 1993 December. This seems to occur just after the second radio burst component is peaking. According to Valtaoja & Teräsranta (1995) EGRET detections occur in general during the rising part of the 22 and 37 GHz radio flare, and once the radio reaches its peak, the gamma radiation ceases.

While it is fair to say that the gamma-ray-bright phase coincides temporally with radio activity, there is no way to prove or disprove the hypothesis of 'related' activity on the basis of the data shown here. Statistically there appears to be good evidence that gamma-ray detections occur during radio outburst rises, but with the undersampling of the gamma-ray data one cannot make claims for correlated gamma-radio activity. The entire period discussed here corresponds to a general decline at cm-wavelengths on which some more rapid fluctuations are superposed. Also, note that while 3C 273 is very bright at radio wavelengths, in the gamma-ray region it has been only moderately strong during detections; there is no clear correlation between gamma-ray flux and radio-flux in general.

It is interesting to note that the intensity of 3C 273 appears to have gone through a local, very flat minimum for wavelengths ≤ 1.3mm (Fig. 3, 3rd panel) during the observed increase at 14.5, 22 and 37 GHz and in γ-rays. A χ^2 test shows that the spread in the sub-mm fluxes in the time range MJD 49300 – 49400 is consistent with constant fluxes even for the 1.1 mm data (Fig. 4). However, the period just before and during the first part of the gamma outburst was not observed because of sun constraints.

In the IR/optical no significant variations have been recorded within the poor sampling throughout the entire period. The range of variations found by Courvoisier et al. (1987) in the optical/IR range was larger, but the average values are compatible. Likewise, the near-IR and optical continuum slopes (as measured by nearly simultaneous JHK, UBV or BVRI sequences) remained constant throughout the period and comparable to the

average slopes. During several epochs with non-photometric conditions variations on short time-scales were searched for by differential photometry (comparing fluxes to constant stars within the same frames). These data had a sampling of about 1 hour^{-1}. They are not flux calibrated and not listed in Table 5. No indications for rapid variations in V and R were found to a level of 1.2 %.

4.2.   Multifrequency Spectrum

Unfortunately, not all of the multiwavelength observations were truly simultaneous with the EGRET observations between 1993 October 19 and 1994 January 3 (MJD 49279 - 49355). For example, the closest IUE data available are from 1994 January 8 (MJD 49360; see Table 6) and the OSSE spectrum is from 1993 December 20 to 27 (MJD 49341 – 49348; Table 7). Anyway, one should bear in mind that the time spans involved in deriving a spectrum from a source are very different from one wavelength range to the other. In the γ-ray range for example the spectrum has been derived from data accumulated over at least one week, while in the other wavelength ranges spectra can be derived on timescales of one day and less. For this reason alone the γ-ray spectrum can never be truly simultaneous to the other multiwavelength spectra. In order to be truly simultaneous the sampling times should be of the same order.

The overall spectrum of 3C 273 during the phase 3 observations (Fig. 5) is similar to that during 1991 June (VP 3) in phase 1 (Lichti et al. 1995). The multiwavelength energy density spectrum (νF_ν spectrum) shows probably four maxima: the first around $3 \cdot 10^{11}$ Hz (corresponding to the mm — sub-mm range), the second maximum (although not observed) must be between 10^{12} Hz and $\approx 10^{14}$ Hz, the third maximum is the "blue bump" at about $3 \cdot 10^{15}$ Hz and the fourth maximum is reached in the MeV region between 1 and 10 MeV. It is the first maximum, in the mm – sub-mm range, which was at a relatively low level during the γ-ray 'flare'. So far, it is not at all clear whether this observation fits the theoretical explanations for the production of the high energy γ-rays.

In order to determine the break energy and the change in spectral index between the hard X-rays and the high energy γ-rays, the energy spectrum beyond 2 keV has been fitted with the same broken power law already used by Lichti et al. (1995). The measured energy spectrum is rather well represented by the following (empirical) function (Fig. 6; the reduced χ^2 for this fit is $\chi^2/dof = 1.04$ with 15 degrees of freedom):

$$F_\nu = (1.66 \pm 0.87) \cdot 10^{-4} \frac{(E/E_b)_{MeV}^{-(0.629 \pm 0.038)}}{1 + (E/E_b)_{MeV}^{(0.97 \pm 0.07)}} \; [mJy]$$

Where E_b has a value of (2.36 ± 1.28) MeV. The fit function indicates a steepening of the energy spectrum by 0.97 ± 0.07 for E >> 2 MeV. This is somewhat more than the value from Lichti et al. (1995) which was 0.8 ± 0.03 for E >> 1 MeV (Fig. 6).

4.2.1. Model fits

In order to test the different models for the generation of γ-rays in the jets of AGN we have fitted the observed spectrum with (i) a synchrotron self-Compton (SSC) model, (ii) an external Compton (EC) model, and (iii) a proton-initiated cascade (PIC) model. The basic assumptions for the jet in all these models are the same as in Blandford & Königl (1979): a conical relativistic and magnetized jet in which accelerated electrons produce a flat radio synchrotron spectrum (owing to a synchrotron-self-absorption turnover frequency decreasing inversely proportional to the jet radius) breaking by one power in the mm-to-infrared range due to energy losses steepening the accelerated electron spectrum.

(i) The SSC model: The relativistic jet SSC calculations are described by Marscher and Travis (1996). The jet is modeled as a truncated cone with a power-law electron spectrum injected at the inner radius. The density falls off as $1/r^2$, the magnetic field as $1/r$, and the electron energies decay from adiabatic, synchrotron, and inverse Compton losses. This provides a smooth-jet approximation to the knotty structure observed with VLBI.

For the model fit, the following parameters have been fixed: Opening half-angle of the jet $(0.5°)$, angle between the jet axis and the line of sight $(6°)$, bulk Lorentz factor 9.3, minimum injected electron energy corresponding to $\gamma_{min} = 100$. The following parameters were determined by the fitting procedure: Injected power-law of electron energy distribution s = 2.3, ratio of randomly oriented to axial component of magnetic field: 1.5; the values at the injection point of the parameters that change with radius are: Cross-sectional radius r = 0.055 pc, magnetic field B = 0.023 G, density of relativistic electrons $n_e = 180$ cm^{-3}, and the maximum injected electron energy $\gamma_{max} = 2.5 \cdot 10^4$.

Hence, 6 parameters were varied until a good fit (Fig. 7) was obtained. We required that the model fit the self-absorption turnover frequency and the overall spectral shape. This places strong constraints on the values of the critical parameters. Nevertheless, we cannot be certain that the fit is the best one possible. The χ^2 for this fit is 270 with 22 degrees of freedom. This applies to the frequency range $3.7 \cdot 10^{10}$ to $2 \cdot 10^{14}$ Hz and $1 \cdot 10^{18}$ to $1 \cdot 10^{24}$ Hz. There was no attempt to fit the optical-UV spectrum, since it is obviously dominated by the big blue bump. The main contributions to the high χ^2 are several points that are poorly fit but have very low observational uncertainty. The χ^2 test indicates that

the fit is not particularly good in detail. However, we are only using an ideal model with a small number of free parameters that can provide a global fit rather than a more complex model designed to fit each point as closely as possible.

We therefore conclude that an SSC-emitting relativistic jet model can reproduce the general shape of the multiwaveband spectrum of 3C 273. This is true even though the physics of the energy losses and radiative transfer are fixed ab initio.

(ii) The EC-model: In this model, the (steady) electron distribution $N(\gamma)$ has been derived using the continuity equation as well as considering cooling, escape, pair production etc. (Ghisellini et al. 1996). In this case one obtains a broken power law because electrons below the minimum injected γ_{min} have a γ^{-2} distribution, while electrons above γ_{min} have $\gamma^{(-s-1)}$, where s is the slope of the injected electrons. In this case it is assumed that electrons are injected continuously, with a power law energy distribution with slope $s = 3.3$ between $\gamma_{min} = 80$ and $\gamma_{max} = 10^4$. This results in an equilibrium distribution which is a broken power law, with index 2 for $\gamma < \gamma_{min}$, and around 4.3 above. The blob sees photons coming from outside, [i.e. photons from the broad line region (BLR)], distributed as a diluted blackbody.

Figure 8 shows the result of the fit of this model to the data. The parameters of the model are: Dimension of the source $R = 2 \cdot 10^{16}$ cm, magnetic field $B = 5.9$ G, injected luminosity $L_i = 3.7 \cdot 10^{44}$erg/s (intrinsic), beaming factor $D = 6.5$ (assumed to be equal to the bulk Lorentz factor) and the ratio of external radiation energy density to magnetic energy density $U'_{ext}/U_B = 11/5.5 = 2$ (in the comoving frame of the blob). The blackbody in the figure corresponds to the relevant disk emission, which illuminates the BLR. The χ^2 for this fit [considering only the points above $\log(\nu)=15$, and excluding the point in the soft X-rays at $\log(\nu)=16.477$], is 108.84. Assuming 6 interesting, adjustable parameters (R, B, γ_{min}, γ_{max}, slope of the injected electron distribution, and R_{BLR}), the reduced χ^2 for this fit is $\chi^2/dof = 7.78$.

The Compton spectrum is not completely smooth, because it is the sum of internal SSC and external Compton. One can see the contribution of the internal SSC at $\nu \sim 10^{16}$ Hz. Electrons with $\gamma < 100$ emit self–absorbed synchrotron radiation, and therefore one does not see the synchrotron emission of the electrons below the break.

Due to the simplicity of this one–zone, homogeneous model, we made no attempt to fit the radio, the far IR and the soft X–ray excess emission. Additional, larger, non-thermal components are needed to model the far IR and the radio data, and another (maybe thermal) component must be responsible for the soft–ray excess. Furthermore, there is no intention to model the UV–bump emission correctly with some theory.

The value of the derived χ^2 can be considered only a very rough measure of the goodness of the fit, given the simplicity of the model, the maybe unrealistically small error bars on some data points (especially in the MeV band) and the fact that not all data points are strictly simultaneous.

(iii) PIC-model: Figure 9 shows a fit to the 3C 273 multifrequency data adopting the proton blazar model (Mannheim 1993b). In this model, γ-rays emerge as the end-product of cascades initiated by ultra-relativistic protons suffering inelastic collisions with low energy synchrotron photons, which appear in the proton rest frame with energies above threshold for secondary pair and pion production. The proton-initiated emission is treated in a one-zone approximation in which the cascades are assumed to occur only at the jet radius where the infrared synchrotron photons (acting as a target for the ultra-relativistic protons) become optically thin. In the present model fit, the jet radius computed from the fit parameters is $r_\perp = 10^{17}$ cm (the distance to the central black hole is undetermined).

Fitting the low energy part of the spectrum as electron synchrotron emission yields a jet Lorentz factor $\gamma_j = 8$, angle to the line-of-sight $\theta = 7°$, opening angle of the jet $\Phi' = 2°$ and a relativistic particle luminosity $L_j = 1.4 \times 10^{46}$ ergs s^{-1}. The proton-to-electron ratio was forced to be $\eta = 100$ allowing for a calculation of the equipartition magnetic field strength $B'_{eq} = 0.8$ G and the synchrotron break frequency in the comoving frame $\nu'_b = 2 \times 10^{10}$ Hz.

Fitting the high-energy part of the spectrum yields the ratio of the proton and electron cooling rates ($\xi = 0.15$) considering that the cascade luminosity emerging in the X-ray and γ-ray bands equals $L_p = \eta \xi L_e$ where L_e denotes the primary electron synchrotron luminosity (radio-to-UV). From the value of ξ, one obtains a proton maximum Lorentz factor of $\gamma_{p,max} = 3 \times 10^{10}$.

In addition to the jet spectrum, an accretion disk spectrum with $S_\nu \propto \nu^{+1/3}$ in the optical-to-UV range has been assumed. The inferred thermal-to-nonthermal luminosity ratio is of order unity. The disk spectrum turns over steeply at 20 eV turning into a power law $S_\nu \propto \nu^{-2}$. This kind of soft X-ray spectrum is expected to emerge from a disk covered by a marginally optically thick jet base (Mannheim, Schulte, & Rachen 1995).

Also γ-ray attentuation by interaction of the jet γ-rays with photons from the jet environment has been taken into account. This is important, since the proton blazar spectrum tends to overproduce γ-rays above ~ 100 MeV, and especially at TeV energies. In the fit, attenuation by diffuse intergalactic light and by scattered disk radiation has been taken into account. The former leads to a quasi-exponential cutoff at $\sim 7 \times 10^{11}$ eV (Mannheim et al. 1996), the latter is characterized by an optical depth

$\tau_{\gamma\gamma} = 0.01(\epsilon/100\,\mathrm{MeV})^{1/2}L_{46}\tau_{-2}$ (Dermer & Schlickeiser, 1994) leading to a steepening by $\Delta s = 0.5$ in the GeV range ($L_{46} = 3$, $\tau_{-2} = 5$). Thus, although in the proton blazar model γ-rays could in principle be produced at an arbitrary distance from the central black hole (provided that the jet is collimated enough to produce infrared synchrotron photons of high density), the spectrum of 3C 273 indicates that the flux of γ-rays is attenuated by traversing the central radiation field. The occasionally observed flattening of the γ-ray spectrum is naturally explained as the signature of a γ-ray emitting shock traveling along the jet away from the central source of thermal radiation, thereby experiencing a decreasing external pair creation optical depth.

Owing to the coarse construction of the model, fine details of the spectrum in the radio-to-infrared and optical-to-UV bands are not well reproduced. They could be fitted with much higher accuracy taking into account jet inhomogeneities and an accretion disk for which published models exist. Such refinements for the proton-initiated cascade part of the model would probably also remove the significant residual at 1-10 MeV which is responsible for the moderate $\chi^2/\nu = 32/20$ of the fit in the X-ray-to-γ-ray regime.

5. Discussion

The increase in γ-ray flux is much slower for 3C 273 than that observed from 3C 279 during its 1991 June flare where the flux increased by a factor of 4 within about 7 days (Kniffen et al. 1993). On the other hand the difference in peak flux from the two sources is about a factor of 7. While in 3C 279 we may have seen only the top of the flare, it is more likely that in the case of 3C 273 we have seen only the initial rise of a flare. One could therefore argue that a γ-ray flare might consist of two parts: a slowly increasing part (as observed in 3C 273) followed by a more eruptive part with a steep decrease at the end as observed in 3C 279 (Kniffen et al. 1993). Such an eruptive part could have easily fit into the two weeks following 1993 December 1 when 3C 273 was not observed by EGRET.

But it could also be that the shape and intensity of the flare is related to the temporal behaviour at lower frequencies: In the case of 3C 279 there was a possible correlation of the γ- ray flare with a short synchroton flare in the R-band (McHardy et al. 1996, Hartman et al. 1996) while in the case of 3C 273 the increase in flux might have been correlated with the much slower second radio outburst components at 22 and 37 GHz. A similar behavior was observed for the quasar PKS 0528+134 where also a radio outburst at 22 and 37 GHz followed the γ-ray flare (Pohl et al. 1995, Mukherjee et al. 1996). Further flares have to be observed before any of these hypotheses can be confirmed.

As already noted by Courvoisier et al. (1987, 1990) the temporal behaviour is very complex in all wavebands with a few correlations, none conclusive mainly because the light curves are undersampled in most cases (especially at shorter wavelengths). Our observations are no exception. From the temporal behavior of 3C 273 during this observational campaign across the entire electromagnetic spectrum one cannot deduce any correlation or anti-correlation of the high energy end with the lower energies, except maybe for the 14.5 GHz, 22 and 37 GHz regime. Statistical investigations of the temporal behavior of *all* the γ-ray emitting AGN seem to support a relation with the 22 and 37 GHz regime (Valtaoja & Teräsranta 1995, Mücke et al. 1996b) although there is no one-to-one correlation.

The decrease of the flux in the sub-mm and mm-regime during the flux increase in the γ-ray regime is probably coincidential, but still represents a problem for the homogeneous SSC models in which changes in intensity (though different in amount) should go in the same direction for all frequencies.

Courvoisier et al. (1987, 1990) already excluded the homogeneous SSC models for 3C 273 because of the lack of mm-X-ray correlations at zero lag[2]. They concluded that this lack of correlation could only be explained with either two different electron components (one for the synchrotron, one for the X-rays) *OR* a second source of photons which dominates the photon energy density in the synchrotron region. This second source of photons would naturally be explained by the EC-models, the second electron component would naturally follow from the proton-induced cascade models where the X- and γ-rays can be produced by completely different particle populations.

Although the increase of the γ-ray intensity was larger than the increase in the synchrotron emission (except for the decrease in the sub-mm and mm-regime), which is qualitatively consistent with the expectations from the SSC models (e.g. Maraschi et al. 1994), the SSC model has to assume either inhomogeneous emission regions or a broken power law for the spectrum of the relativistic electrons (Ghisellini et al. 1996) in order to account for the – in general – two peaks (one in the IR-optical and one in the γ-ray regime (see e.g. von Montigny et al. 1995)) in the overall spectral energy distribution of the γ-ray emitting AGN. 3C 273 has at least three (maybe even four) peaks in its spectral energy distribution, indicating an even more complicated situation and maybe even as many as four different emission mechanisms (Courvoisier et al. 1987).

The attempts of fitting the observed multiwavelength spectrum of 3C 273 with theoretical models also show that the spectrum can not be well represented without

---

[2]Another very prominent quasar for which such a lack of mm-X-ray correlation is known is 3C 345 (Bregman et al. 1986)

the contribution of several components. For example, the "big blue bump" peaking at $\approx 3 \cdot 10^{15}$Hz may be indicating the presence of a massive accretion disk providing copious possible target photons for the relativistic particles in the jet. All three models are capable of representing the MeV-Bump within the errors. In the X-ray/γ-ray range, the data cannot be fit well by a smooth SSC spectrum within the 1 σ error bars but including the big blue bump and first order Comptonization of these photons might improve the situation in that regime. The EC-model has some difficulties to account for the low energy range between $10^9 < \nu < 10^{14}$ and also the extreme UV range without assuming at least additional emission sites. The PIC-model yields the best overall fit of the multiwavelength spectrum over more than 17 decades with only three necessary components. Another possibility to generate the high γ-ray emission which has not been mentioned yet is the Comptonization of the "big blue bump" by a monoenergetic relativistic electron outflow involving multiple inverse Compton scattering (Titarchuk & Lyubarskij 1995, Ramos et al. 1996).

Although this campaign has the by far best coverage across the entire electromagnetic spectrum the data are still insufficient to discriminate between all the possible emission models for the high γ-ray emission. What is still missing is a truly *simultaneous* and *regular* monitoring of 3C 273 (and other blazars) at all frequencies before, during and after a flare in high energy γ-rays. The more we learn about 3C 273 and other γ-ray emitting quasars the more it is becoming evident that 3C 273 is far from being a standard quasar.

REFERENCES

Aller, H.D. et al. 1985, ApJS, 59, 513.

Bertsch, D.L. et al. 1993, ApJ, 416, 587.

Bignami, G.F. et al. 1981, A&A, 93, 71.

Blandford, R.D. & Königl, A. 1979, ApJ, 232, 34.

Bloom, S.D. & Marscher,A.P. 1992 in The Compton Observatory Science Workshop, ed. C.R. Shrader, N. Gehrels, & B. Dennis (NASA CP 3137), 339.

Bloom, S.D. & Marscher,A.P. 1993 in AIP Conf. Proc. No. 280, Proc. Compton Symp., ed. M. Friedlander, N. Gehrels, & D. J. Macomb (New York:AIP), 578.

Bowyer, C.S. et al. 1970, ApJ, 161, L1.

Bregman, J.N. et al. 1986, ApJ, 301, 708.

Chiang, J. et al. 1995, ApJ, 452, 156.

Conway, J.E. et al. 1982, in IAU Symp. 97, Extragalactic Radio Sources, (Dordrecht:Kluwer), 167.

Courvoisier, T.J.-L. et al. 1987, A&A, 176, 197.

Courvoisier, T.J.-L. et al. 1988, Nature, 335, 330.

Courvoisier, T.J.-L. et al. 1990, A&A, 176, 197.

de Boer, H. et al. 1992, in Data Analysis in Astronomy IV, ed. V. di Gesu et al. (New York:Plenum Press), 241.

Dermer, C.D., Schlickeiser, R., & Mastichiadis, A. 1992, A&A, 256, L27.

Dermer, C.D. & Schlickeiser, R. 1994, ApJS, 90, 945.

Dingus, B.L. et al. 1996, ApJ, 467, 589.

Dondi, L. & Ghisellini, G. 1995, MNRAS, 273, 583.

Duncan, W.D. et al. 1990, MNRAS, 243, 126.

Eadie, W.T. et al. 1971, in Statistical Methods in Experimental Physics, ed. North-Holland Publ. Co.

Fichtel, C.E. et al. 1994, in AIP Conf. Proc. No. 304, Proc. 2nd Compton Symp., ed. C.E. Fichtel, N. Gehrels & J.P. Norris (New York:AIP), 721.

Ghisellini, G. et al. 1996, A&AS, 120, 503.

Harris, D.E. & Stern, C.P. 1987, ApJ, 313, 136.

Hartman, R.C. et al. 1996, ApJ, 461, 698.

Hermsen, W. et al. 1981, Proc. 17th Int. Cosmic Ray Conf. (Paris), 1, 230.

Hermsen, W. et al. 1993, A&AS, 97, 97.

Hunter, S.D. et al. 1996, ApJ, submitted.

Impey, C. D. et al. 1989, ApJ, 347, 96.

Johnson, W.N. et al. 1993, ApJS, 86, 693.

Johnson, W.N. et al. 1995, ApJ, 445, 182.

Kanbach, G. et al. 1988, Space Sci. Rev., 49, 69.

Kniffen, D.A. et al. 1993, ApJ,411, 133.

Kühr, H. et al. 1981, A&AS, 45, 367.

Lichti, G.G. et al. 1994, in IAU Symp. 159, Active Galactic Nuclei across the Electromagnetic
       Spectrum, ed. T. Courvoisier & A. Blecha (Dordrecht:Kluwer), 327.

Lichti, G.G. et al. 1995, A&A, 278, 711.

Makishima, K. et al. 1996, PASJ, 48, 171.

Mannheim, K. 1993a, Phys. Rev. D, 48, 2408.

Mannheim, K. 1993b, A&A, 269, 67.

Mannheim, K. & Biermann, P.L. 1992, A&A, 253, L21.

Mannheim, K. et al. 1996, A&A, in press.

Mannheim, K., Schulte, M., & Rachen, J. 1995, A&A, 303, L41.

Maraschi, L. et al. 1994, ApJ, 435, L91.

Maraschi, L., Ghisellini, G., & Celotti, A. 1992, ApJ, 397, L5.

Marscher, A. & Travis, J.P. 1996, A&AS, 120, 537.

Mattox, J.R. et al. 1996, ApJ, 461, 396.

McHardy, I. et al. 1996, in preparation.

McNaron-Brown, K. et al. 1994, in AIP Conf. Proc. No. 304, Proc. 2nd Compton Symp., ed. C.E. Fichtel, N. Gehrels, & J.P. Norris (New York:AIP), 587.

Mücke, A. et al. 1996, in Extragalactic Radio Sources, IAU Symposium 175, Kluwer, Dordrecht, in press.

Mücke, A. et al. 1996, A&AS, 120, 541.

Mukherjee, R. et al. 1996, ApJ, in press.

Paciesas, W.S. et al. 1994, in AIP Conf. Proc. No. 304, Proc. 2nd Compton Symp., ed. C.E. Fichtel, N. Gehrels, & J.P. Norris (New York:AIP), 674.

Pohl, M. et al. 1995, A&A, 303, 383.

Ramos, E. et al. 1996, ApJ, 482, in press.

Reich, W. et al. 1993, A&A, 273, 65.

Robson, E.I. et al. 1993, MNRAS, 262, 249.

Schönfelder, V. et al. 1993, ApJS, 86, 657.

Schmidt, M. 1963, Nature, 197, 1040.

Seaton, M.J. 1979, MNRAS, 187, 73P.

Sikora, M., Begelman, M.C., & Rees, M.J. 1994, ApJ, 421, 153.

Sreekumar, P. et al. 1996, ApJ, 464, 628.

Swanenburg, B.N. et al. 1978, Nature, 275, 298.

Teräsranta, H. et al. 1992, A&AS, 94, 121.

Thompson, D.J. et al. 1993, ApJS, 86, 629.

Thompson, D.J. et al. 1995, ApJS, 101, 259.

Thompson, D.J. et al. 1996, ApJS, 107, in press.

Titarchuk, L. & Lyubarskij, Y. 1995, ApJ, 450, 876.

Tornikoski, M. et al. 1996, A&AS, 116, 157.

Valtaoja, E. & Teräsranta, H. 1995, A&A, 297, L13.

Valtaoja E. et al. 1990, AJ, 99, 769.

Valtaoja L. et al. 1991, AJ, 102, 1946.

von Montigny, C. et al. 1995, ApJ, 440, 525.

von Montigny, C. et al. 1993, A&AS, 97, 101.

Williams, O.R. et al. 1995, A&A, 298, 33.

Fig. 1.— Comparison of spectra of 3C 273 during VP 305.0 (asterisks) and VP 308.6 (squares). It can be seen that the increase in flux comes from a hardening of the spectrum.

Fig. 2.— Spectral indices versus integral flux above 100 MeV for 3C 273. There is evidence that the γ-ray spectra harden with increasing flux.

Fig. 3.— Time histories of 3C 273 .

Fig. 4.— mm- and sub-mm fluxes of 3C 273 during the EGRET observations.

Fig. 5.— Quasi-simultaneous multiwavelength spectrum of 3C 273. The data in the radio through UV range have not been averaged.

Fig. 6.— High energy spectrum of 3C 273 . The solid line is the result from the fit in this paper and the dashed line is the fit from Lichti et al. (1995).

Fig. 7.— Fit of the SSC-model to the observed spectrum of 3C 273 . Parameters of the model are: cross-sectional radius r = 0.055 pc, opening half-angle of the jet: 0.5°, angle between the jet axis and the line of sight: 6°, bulk Lorentz factor: 9.3, minimum injected electron energy $\gamma_{min} = 100$, maximum injected electron energy $\gamma_{max} = 2.5 \cdot 10^4$, injected power-law of electron energy distribution: 2.3, density of relativistic electrons $N_e = 180$ cm^{-3}, magnetic field B = 0.023 G, ratio of randomly oriented to axial component of magnetic field: 1.5.

Fig. 8.— Fit of the EC-model to the observed spectrum of 3C 273 . Parameters of the model are: Dimension of the source R = $2 \cdot 10^{16}$ cm, magnetic field B = 5.9 G, injected luminosity $L_i = 3.7 \cdot 10^{44}$ erg/s, beaming factor D = 6.5, $U_{ext}'/U_B = 2$.

Fig. 9.— Fit of the PIC-model to the observed spectrum of 3C 273 . Parameters of the model are: Jet radius $r_\perp = 10^{17}$cm, jet Lorentz factor $\gamma_j = 8$, angle to the line of sight $\theta = 7°$, relativistic particle luminosity $L_j = 1.4 \cdot 10^{46}$erg/s, proton to electron ratio $\eta = 100$, equipartition magnetic field strength $B'_{eq} = 0.8$ G, ratio of proton and electron cooling rates $\xi = 0.15$, maximum proton Lorentz factor $\gamma_{p,max} = 3 \times 10^{10}$.

log photon energy [eV]
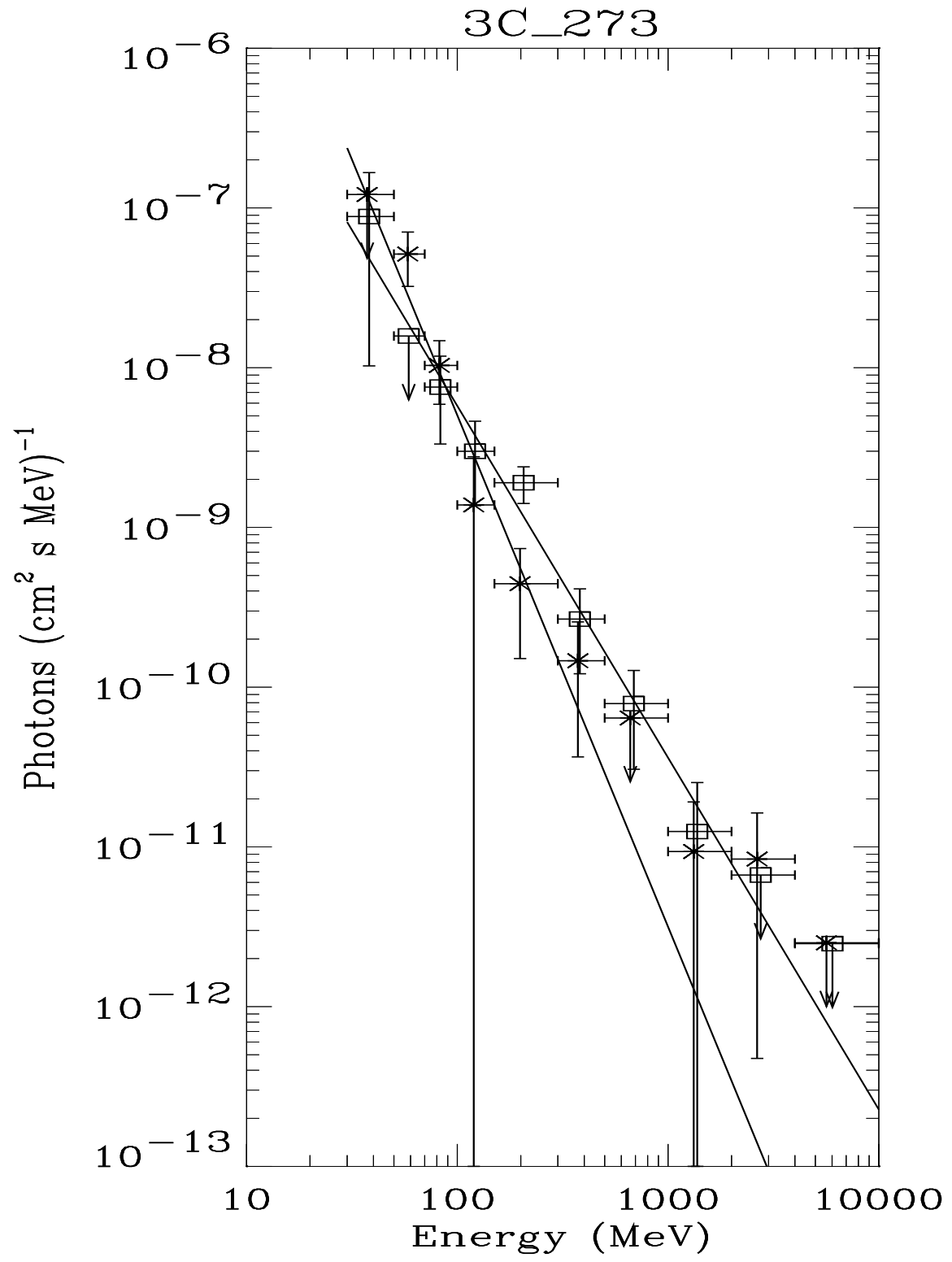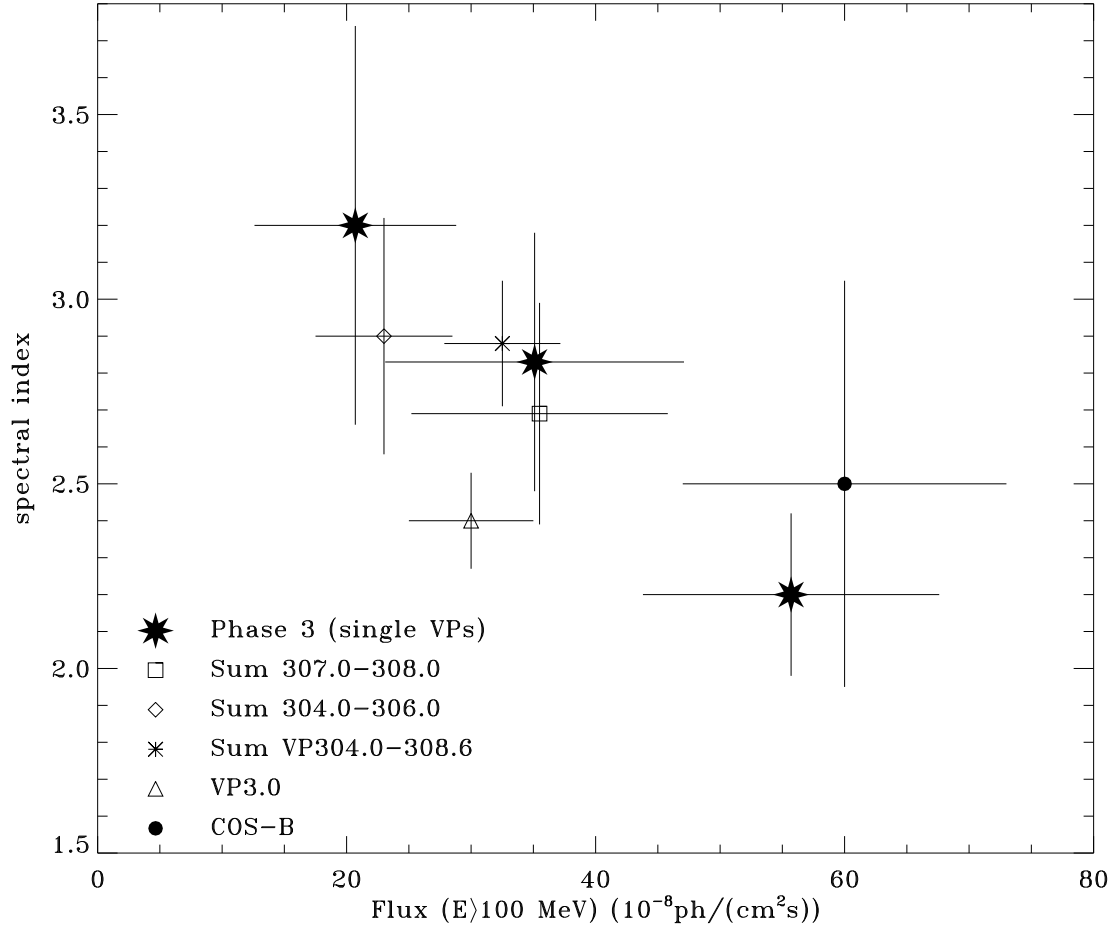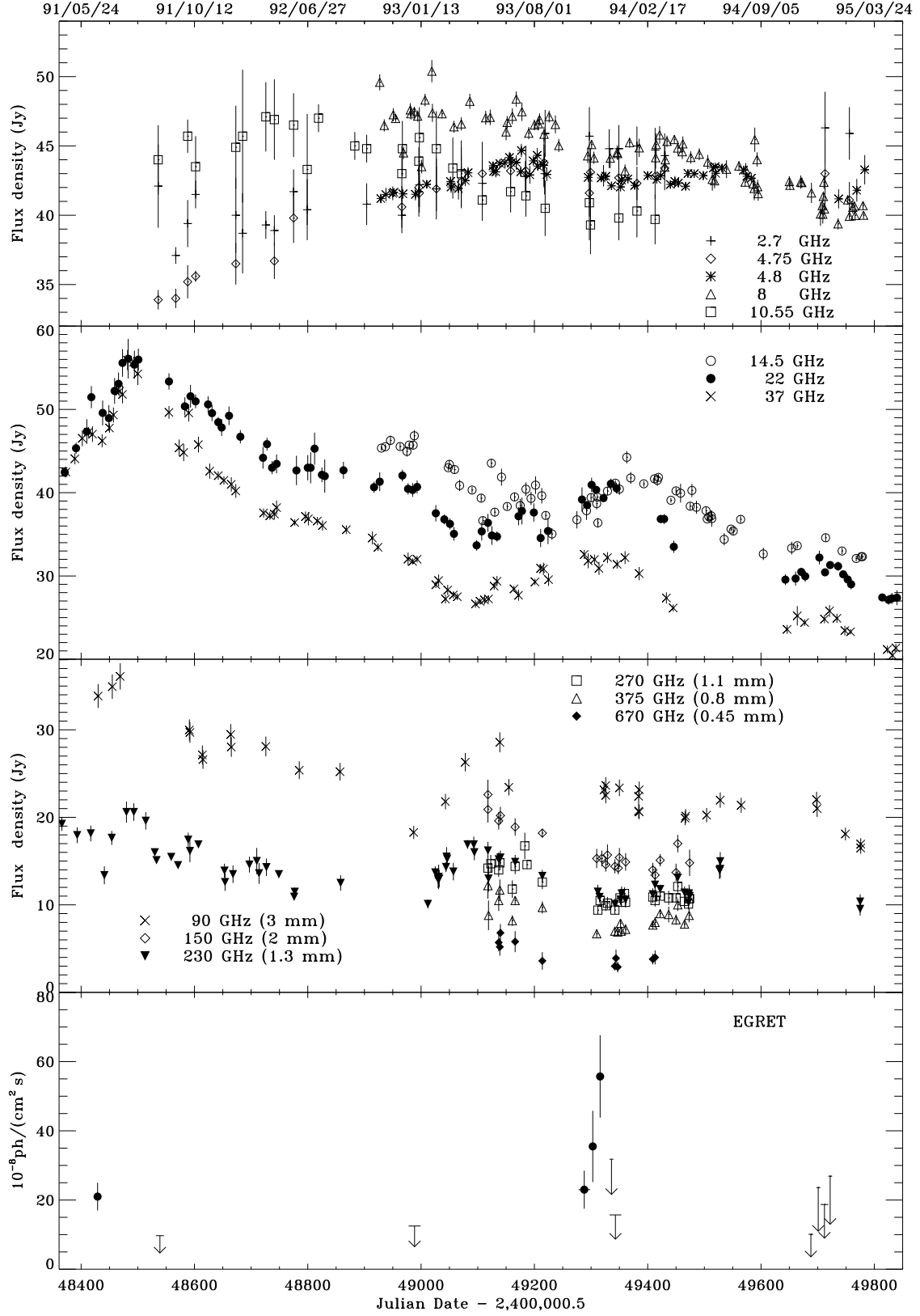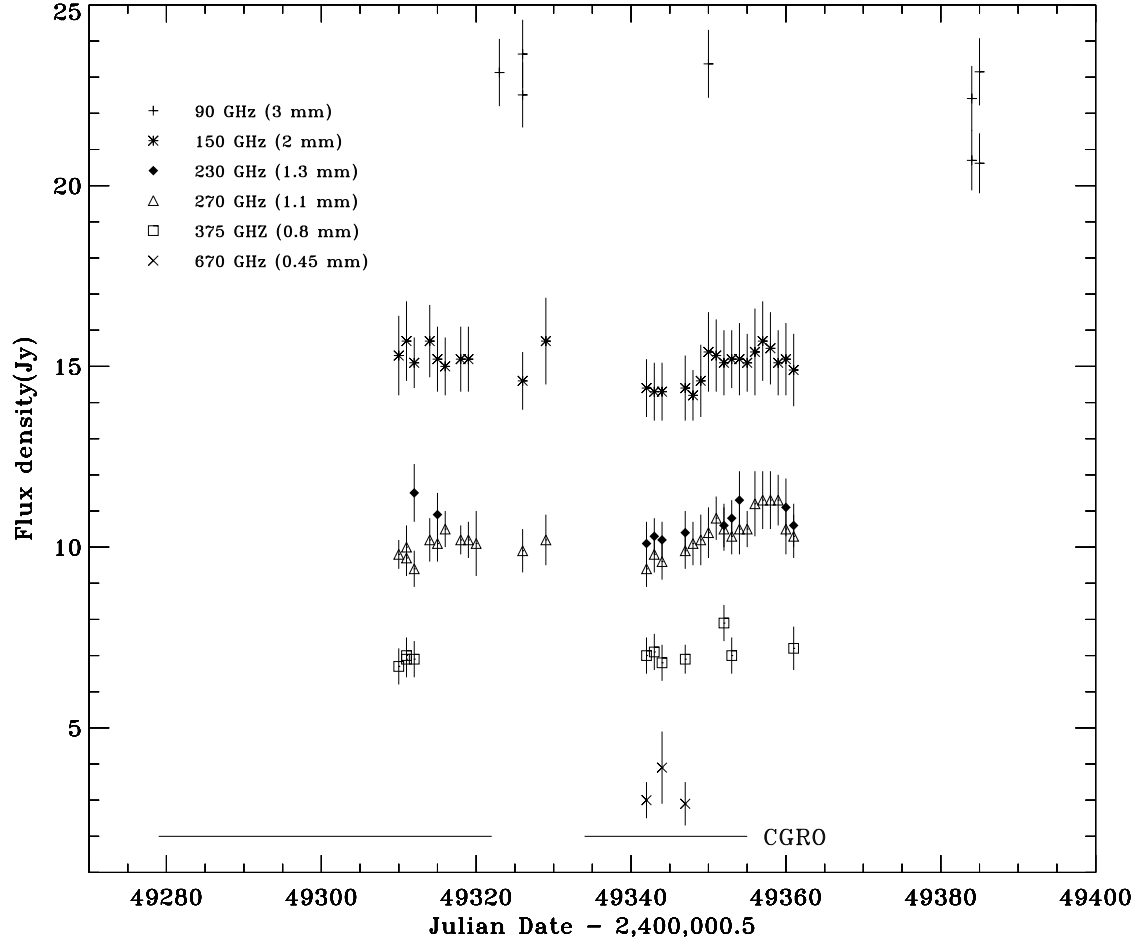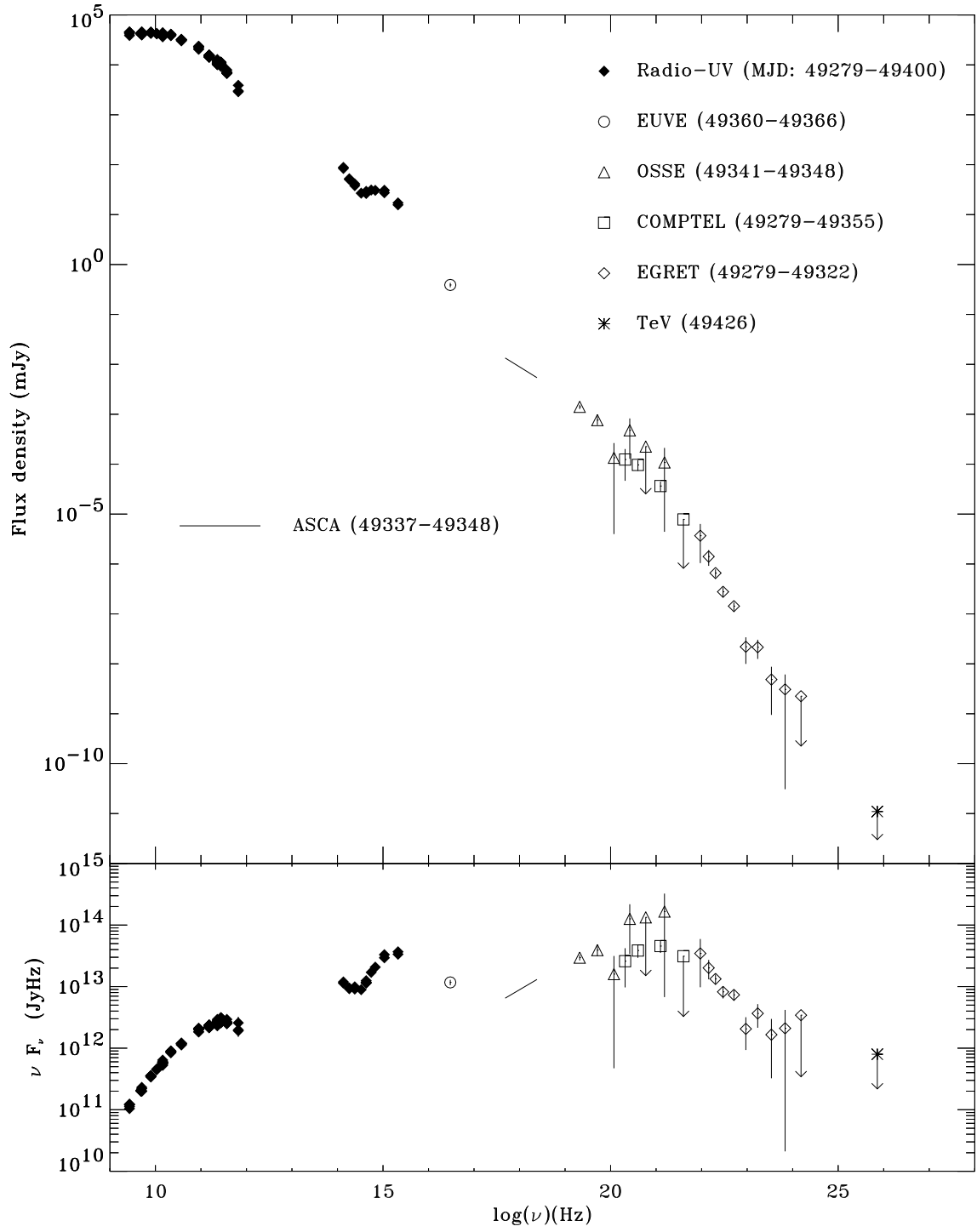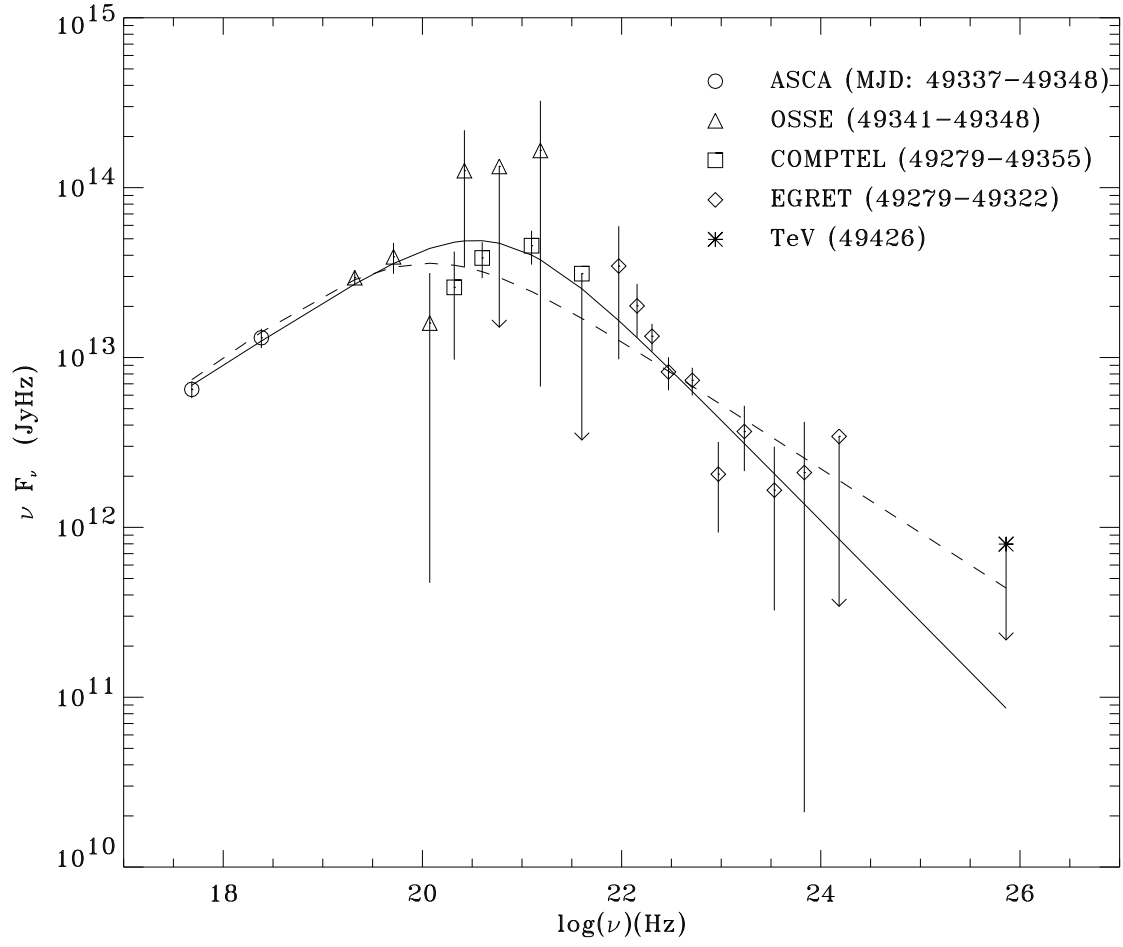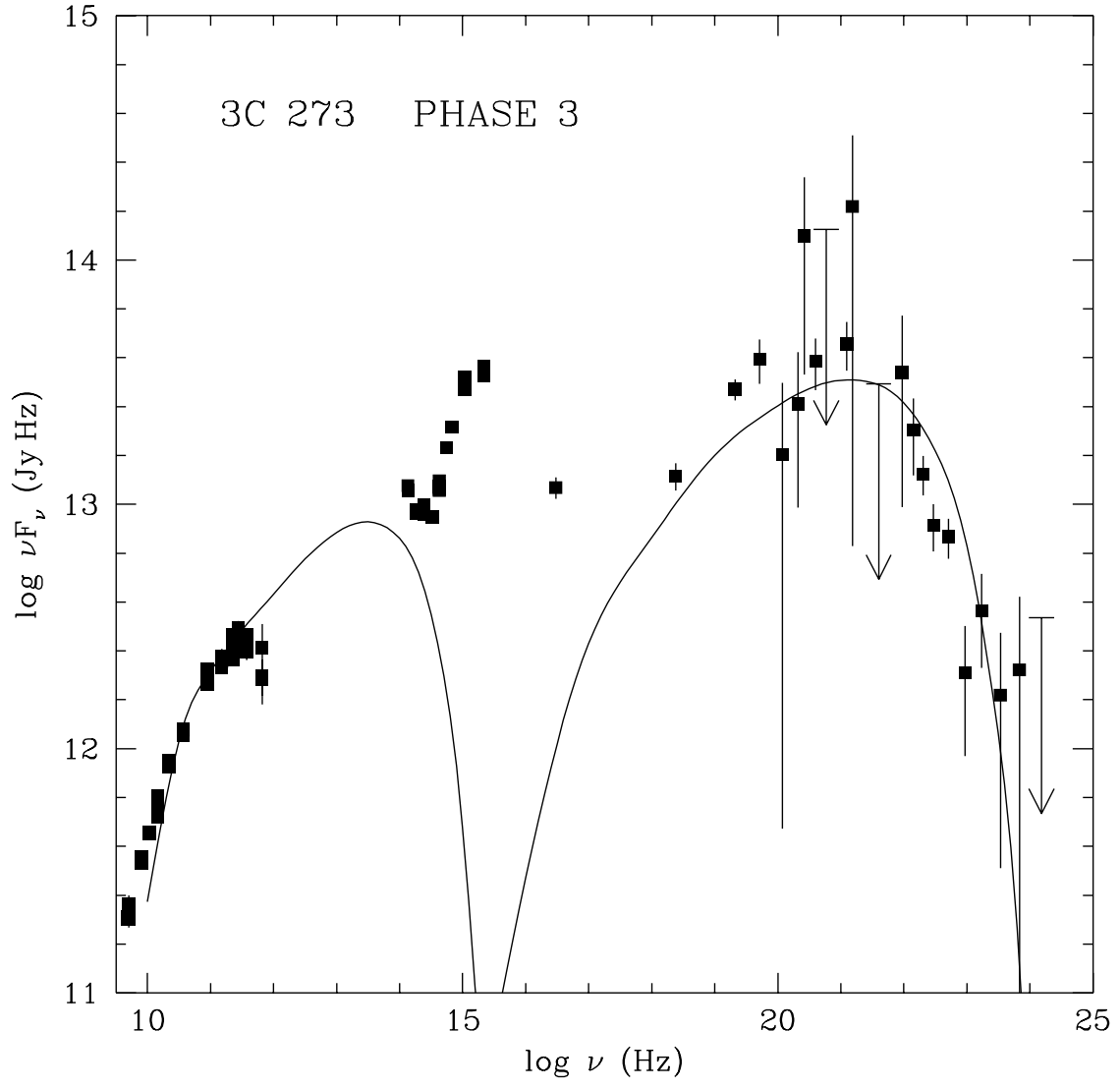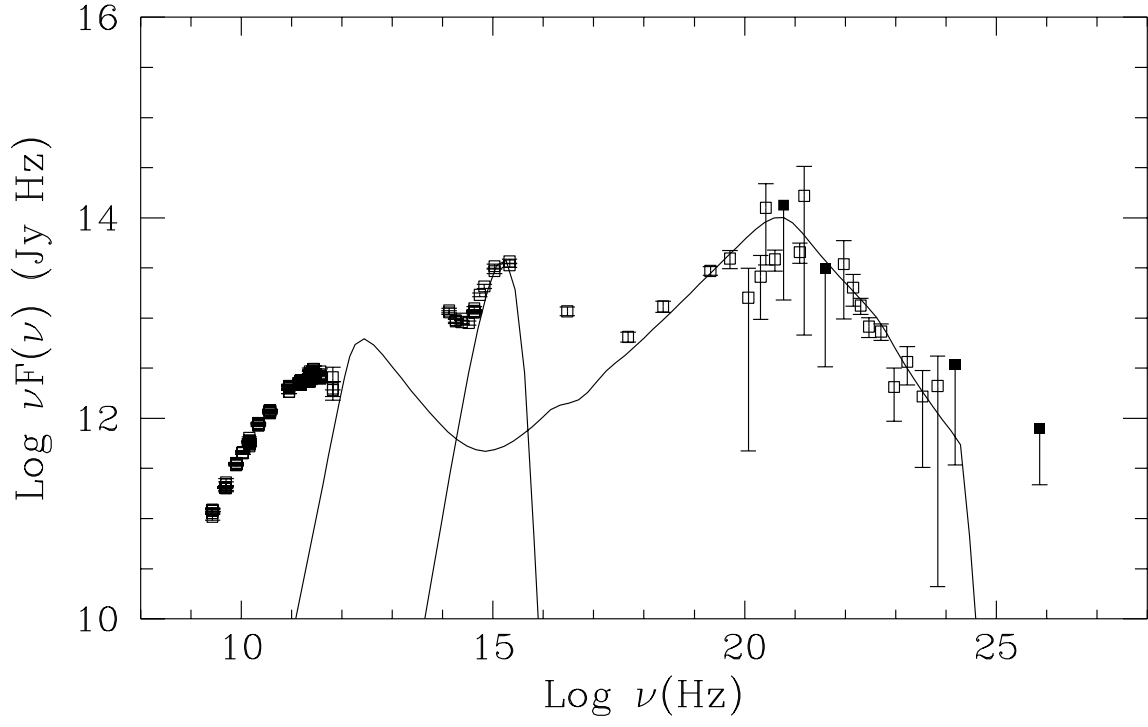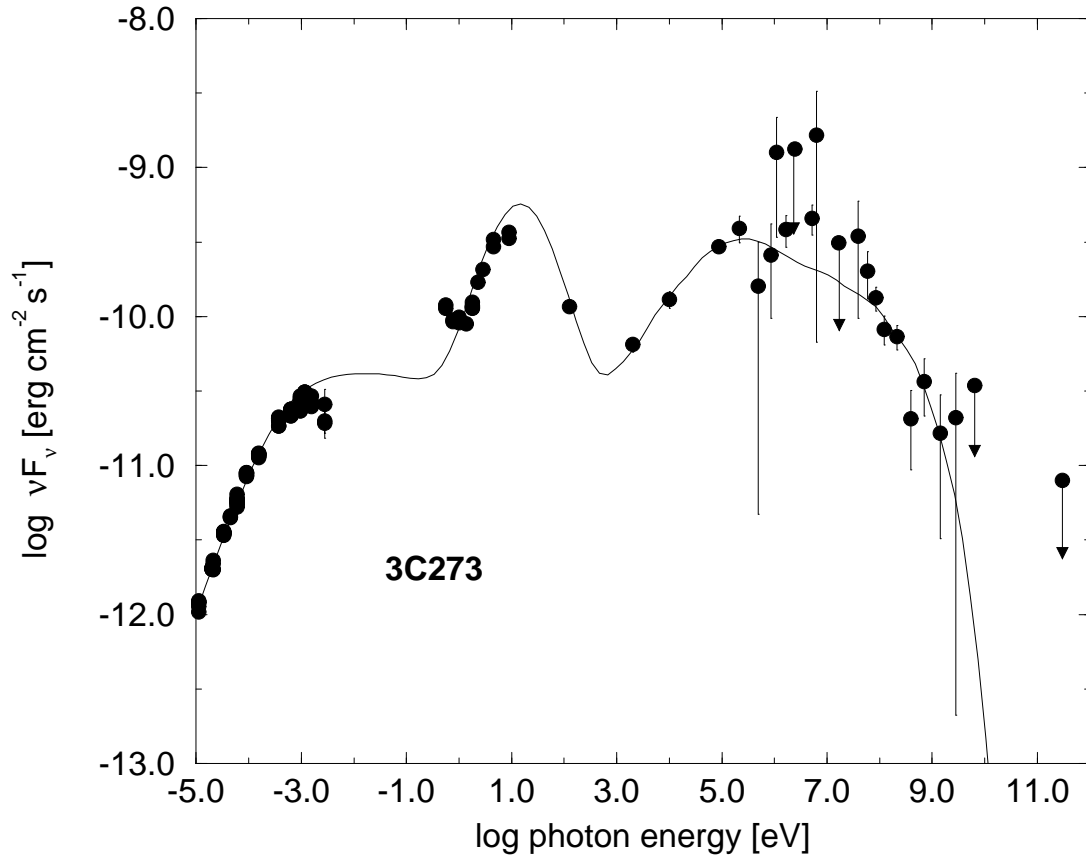
3C273

Table 1.   EGRET fluxes of 3C 273 from phases 1, 2, 3, and cycle 4.

Viewing Period	Time of Observation	MJD	Offset (deg)	Signif. $\sqrt{TS}$	Flux(E>100MeV) (10^{-8}photons cm^{-2}s^{-1})
3.0	06/15/91 - 06/28/91	48422-48435	4.29	6.7	23.8±4.5
11.0	10/03/91 - 10/17/91	48532-48546	2.00	2.5	< 17.7
204.0	12/22/92 - 12/29/92	48978-48685	3.28	0.5	< 18.2
205.0	12/29/92 - 01/05/93	48685-48992	3.46	2.3	< 33.2
206.0	01/05/93 - 01/12/93	48992-48999	3.28	2.5	< 46.5
204.0 ... 206.0	12/22/92 - 01/12/93	48978-48999	· · ·	0.8	< 12.5
304.0	10/19/93 - 10/25/93	49279-49285	5.38	3.0	< 44.0
305.0	10/25/93 - 11/02/93	49285-49293	5.69	3.4	20.7± 8.1
306.0	11/02/93 - 11/09/93	49293-49300	8.14	2.8	< 42.0
304.0 ... 306.0	10/19/93 - 11/09/93	49279-49300	· · ·	5.4	22.4± 5.3
307.0	11/09/93 - 11/16/93	49300-49307	9.62	4.1	35.1± 12.0
308.0	11/16/93 - 11/19/93	49307-49310	10.54	2.3	< 68.0
307.0 ... 308.0	11/09/93 - 11/19/93	49300-49310	· · ·	4.7	34.0± 9.9
308.6	11/23/93 - 12/01/93	49314-49322	10.54	6.7	55.7± 11.9
311.0	12/13/93 - 12/15/93	49334-49336	10.37	0.0	< 34.0
311.6	12/17/93 - 12/20/93	49338-49341	10.37	1.7	< 61.0
311.0 ... 311.6	12/13/93 - 12/20/93	49334-49341	· · ·	1.2	< 36.0
312.0	12/20/93 - 12/27/93	49341-49348	7.28	0.4	< 21.6
313.0	12/27/93 - 01/03/94	49348-49355	14.34	0.2	< 23.7
311.6 ... 312.0	12/17/93 - 12/27/93	49338-49348	· · ·	0.1	< 18.9
311.0 ... 313.0	12/13/93 - 01/03/94	49334-49355	· · ·	0.4	< 15.7
405.0	11/29/94 - 12/07/94	49685-49693	11.30	0.0	< 10.1
406.0	12/13/94 - 12/20/94	49699-49706	18.77	0.0	< 23.6
407.0	12/20/94 - 01/03/95	49706-49720	19.33	0.0	< 18.7
408.0	01/03/95 - 01/10/95	49720-49727	10.36	1.6	< 26.9

Table 2.   Results of spectral analysis.

Viewing Period	Spectral Index (Γ_γ)	N_o 10^{-9}photons cm^{-2}s^{-1} MeV^{-1}	E_o MeV	χ^2/n_f
305.0	3.20± 0.54	4.62± 1.23	102.7	0.71
304.0 ... 306.0	2.93± 0.33	1.75± 0.36	123.0	0.46
307.0	2.83± 0.35	6.83± 1.41	110.1	0.35
307.0 ... 308.0	2.69± 0.32	6.84± 1.33	118.4	0.53
308.6	2.20± 0.22	0.96± 0.19	225.7	0.63
304.0 ... 308.6	2.59± 0.15	1.58± 0.18	155.3	0.75

Table 3a.   2.7, 4.75 and 10.55 GHz radio data for 3C 273 (Pohl, Reich).

MJD	2.7 GHz		4.75 GHz		10.55 GHz	
	Flux(Jy)	σ(Jy)	Flux(Jy)	σ(Jy)	Flux(Jy)	σ(Jy)
48335	$\cdots$	$\cdots$	33.40	0.50	$\cdots$	$\cdots$
48536	42.10	3.00	33.90	0.70	44.00	2.50
48567	37.10	0.60	34.00	0.70	$\cdots$	$\cdots$
48588	39.40	1.70	35.20	1.20	45.70	1.20
48602	41.50	1.00	35.60	0.40	43.50	2.20
48673	40.00	2.70	36.50	1.50	44.90	3.00
48685	38.70	2.90	$\cdots$	$\cdots$	45.70	4.80
48726	39.30	1.00	$\cdots$	$\cdots$	47.10	2.50
48741	38.90	1.10	36.70	1.30	46.90	2.90
48775	41.70	1.60	39.80	1.80	46.50	2.30
48799	40.40	2.20	$\cdots$	$\cdots$	43.30	4.00
48819	$\cdots$	$\cdots$	$\cdots$	$\cdots$	47.00	1.00
48883	$\cdots$	$\cdots$	$\cdots$	$\cdots$	45.00	1.00
48904	40.80	1.50	$\cdots$	$\cdots$	44.80	1.00
48966	40.00	1.30	40.60	1.50	43.00	2.00
48967	$\cdots$	$\cdots$	$\cdots$	$\cdots$	44.80	2.00
48996	41.70	1.80	42.00	1.40	43.90	1.00
48997	42.20	1.60	41.60	1.40	45.60	2.20
49027	41.90	1.60	41.90	2.20	44.80	2.70
49056	$\cdots$	$\cdots$	$\cdots$	$\cdots$	43.40	2.20
49071	43.20	1.70	42.40	1.90	43.00	2.40
49108	42.30	1.70	43.00	2.30	41.10	1.50
49158	$\cdots$	$\cdots$	43.20	1.30	41.70	1.50
49184	42.80	1.10	$\cdots$	$\cdots$	$\cdots$	$\cdots$
49185	42.80	1.20	43.20	1.80	41.40	1.50
49217	43.60	1.50	43.80	1.80	$\cdots$	$\cdots$
49218	43.00	1.50	$\cdots$	$\cdots$	$\cdots$	$\cdots$
49219	45.90	1.70	$\cdots$	$\cdots$	40.50	2.00
49297	45.70	2.10	41.60	1.70	40.90	2.70
49299	$\cdots$	$\cdots$	43.10	1.70	39.30	2.10
49332	44.80	1.40	$\cdots$	$\cdots$	$\cdots$	$\cdots$
49349	44.80	1.70	42.70	1.60	39.80	1.60
49381	45.00	1.40	42.30	1.20	40.30	1.90
49413	44.70	1.60	42.80	1.60	39.70	1.80

Table 3a—Continued

MJD	2.7 GHz		4.75 GHz		10.55 GHz	
	Flux(Jy)	σ(Jy)	Flux(Jy)	σ(Jy)	Flux(Jy)	σ(Jy)
49430	44.30	1.60	43.40	1.60	41.50	2.00
49713	46.30	2.60	43.00	2.50	$\cdots$	$\cdots$
49756	45.90	1.90	41.10	1.30	$\cdots$	$\cdots$

Table 3b.   4.8 GHz light curve for 3C 273 (Aller & Aller).

MJD	Flux (Jy)	σ (Jy)
48929	41.20	0.34
48938	41.49	0.49
48950	41.58	0.50
48952	41.65	0.25
48968	41.54	0.34
48990	41.51	0.44
49010	42.23	0.30
49052	42.43	0.36
49053	42.04	0.43
49066	41.93	0.80
49078	42.50	0.40
49083	43.06	0.41
49127	43.57	0.28
49128	43.17	0.28
49132	43.13	0.40
49139	43.73	0.22
49148	43.77	0.41
49156	44.16	0.41
49159	43.78	0.42
49168	43.80	0.52
49176	43.13	0.38
49177	44.67	0.48
49192	42.91	0.64
49198	43.92	0.34
49205	44.32	0.53
49206	43.54	0.31
49215	43.65	0.38
49222	42.94	0.48
49295	42.73	0.23
49318	42.69	0.25
49326	42.81	0.32
49336	42.12	0.26
49352	42.04	0.32
49354	42.53	0.23

Table 3b—Continued

MJD	Flux (Jy)	σ (Jy)
49365	42.62	0.31
49377	42.15	0.24
49400	42.86	0.32
49416	42.59	0.30
49423	42.85	0.24
49440	42.22	0.28
49448	42.43	0.40
49454	42.32	0.21
49467	42.09	0.19
49471	43.01	0.25
49482	42.99	0.25
49498	42.86	0.33
49516	43.42	0.29
49519	43.50	0.19
49520	43.02	0.25
49531	43.41	0.25
49569	43.25	0.27
49575	42.81	0.20
49583	42.67	0.37
49737	41.18	0.69
49769	41.80	0.82
49783	43.28	1.06

Table 3c. 8 GHz light curve for 3C 273 (Aller & Aller).

MJD	Flux (Jy)	σ (Jy)
48927	49.59	0.58
48935	46.48	0.44
48951	47.25	0.47
48955	46.98	0.31
48969	44.50	0.44
48981	47.60	0.48
48982	47.32	0.42
48988	47.47	0.35
48994	47.15	0.40
49001	43.51	0.49
49007	48.31	0.45
49019	50.39	0.80
49020	47.38	0.65
49037	47.32	0.34
49058	46.38	0.43
49071	46.59	0.48
49086	48.22	0.54
49114	47.03	0.51
49122	47.06	0.56
49150	46.01	0.60
49152	46.69	0.46
49161	47.14	0.57
49168	48.38	0.55
49178	47.47	0.67
49190	45.92	0.44
49200	46.51	0.39
49207	46.60	0.48
49209	46.90	0.45
49217	45.84	0.54
49226	47.12	0.43
49237	46.55	0.65
49243	45.03	0.47
49294	44.28	0.51
49301	45.10	0.33

Table 3c—Continued

MJD	Flux (Jy)	σ (Jy)
49305	44.14	0.44
49322	42.85	0.78
49334	44.12	0.72
49346	44.53	0.50
49347	44.45	0.47
49360	43.20	0.46
49368	45.24	0.37
49385	44.86	0.66
49414	44.15	0.79
49415	45.10	0.81
49421	45.79	0.63
49430	43.47	0.51
49431	44.00	0.62
49434	45.33	0.41
49447	45.46	0.33
49453	44.85	0.49
49461	44.58	0.53
49462	45.15	0.53
49476	44.17	0.44
49491	44.40	0.43
49506	43.84	0.51
49514	42.59	0.82
49518	42.49	0.55
49539	43.32	0.65
49561	43.55	0.36
49572	42.39	0.34
49573	43.29	0.48
49586	42.27	0.39
49588	41.93	0.85
49589	45.45	0.87
49593	44.02	0.52
49594	42.06	0.50
49595	41.56	0.51
49650	42.43	0.39

Table 3c—Continued

MJD	Flux (Jy)	σ (Jy)
49651	42.16	0.34
49670	42.39	0.48
49672	42.36	0.37
49689	41.61	0.73
49705	40.09	0.86
49708	40.70	0.57
49709	40.08	0.68
49710	41.36	0.35
49711	42.38	0.48
49712	40.46	0.43
49736	39.38	0.41
49753	41.11	0.34
49756	39.92	0.31
49762	40.57	0.45
49765	40.66	0.33
49766	39.99	0.40
49780	40.70	0.29
49781	40.00	0.27

Table 3d. 14.5 GHz light curve for 3C 273 (Aller & Aller).

MJD	Flux (Jy)	σ (Jy)
48930	45.36	0.30
48937	45.52	0.32
48946	46.28	0.57
48963	45.54	0.40
48975	44.95	0.61
48979	45.72	0.35
48986	45.71	0.44
48988	46.83	0.67
49048	43.00	0.35
49050	43.40	0.53
49059	42.78	0.49
49068	40.86	0.67
49090	40.32	0.38
49106	39.35	0.46
49109	36.65	0.52
49124	43.54	0.50
49130	37.66	0.48
49142	41.87	1.02
49152	38.34	0.39
49165	39.49	0.53
49175	38.45	0.81
49185	40.42	0.81
49194	39.31	0.79
49202	40.91	1.06
49213	39.64	0.93
49220	37.27	0.47
49231	35.05	0.70
49275	36.75	1.04
49292	37.84	1.10
49300	39.41	0.49
49310	38.69	0.69
49311	39.47	0.34
49312	36.38	0.57
49329	40.19	0.48

Table 3d—Continued

MJD	Flux (Jy)	σ (Jy)
49343	41.14	0.36
49350	40.43	0.69
49363	44.25	0.75
49370	41.77	0.71
49393	41.07	0.34
49412	41.67	0.39
49417	41.49	0.67
49419	41.84	0.38
49441	39.09	0.29
49450	40.22	0.41
49458	39.94	1.13
49475	38.38	0.44
49478	40.27	0.79
49486	38.25	0.78
49503	37.83	0.42
49505	36.85	0.28
49508	37.11	0.53
49512	37.22	0.63
49513	36.88	0.97
49535	34.40	0.73
49547	35.63	0.28
49551	35.40	0.48
49564	36.80	0.43
49604	32.65	0.74
49654	33.34	0.77
49664	33.63	0.34
49714	34.59	0.47
49743	33.00	0.38
49768	32.10	0.35
49777	32.32	0.32
49779	32.32	0.40

Table 3e.   22 GHz light curve for 3C 273 (Teräsranta, Tornikoski, Valtaoja).

MJD	Flux (Jy)	σ (Jy)
48305	38.62	0.79
48315	38.16	0.65
48324	40.11	0.63
48357	41.84	0.64
48371	42.45	0.59
48391	45.34	0.68
48410	47.34	1.48
48418	51.47	1.33
48438	49.58	1.49
48449	48.95	1.56
48459	52.22	1.54
48466	53.07	1.36
48473	55.58	1.66
48483	56.09	2.37
48494	55.37	1.68
48501	55.98	1.33
48555	53.36	0.98
48583	50.37	1.09
48593	51.58	1.37
48602	50.97	0.83
48624	50.60	0.97
48631	49.55	0.96
48642	48.46	0.62
48648	47.83	1.02
48661	49.24	1.11
48681	46.72	0.80
48721	44.19	1.30
48728	45.83	0.76
48737	43.00	0.78
48745	43.46	1.13
48780	42.67	1.76
48800	43.00	1.52
48805	42.99	1.87
48812	45.29	1.93

Table 3e—Continued

MJD	Flux (Jy)	σ (Jy)
48825	42.15	0.88
48830	41.99	1.99
48863	42.69	1.02
48917	40.66	0.67
48927	41.32	1.12
48967	42.06	0.70
48977	40.46	0.68
48985	40.33	0.83
48993	40.69	0.78
49026	37.53	0.98
49041	36.80	0.60
49051	36.25	0.66
49058	35.06	0.82
49098	33.68	0.64
49107	35.35	1.09
49118	36.38	1.08
49125	34.86	1.12
49134	34.74	0.61
49172	37.17	1.08
49178	37.80	1.61
49199	37.62	1.09
49211	34.56	1.09
49224	35.40	1.57
49284	39.18	1.46
49293	38.50	0.50
49301	40.94	0.86
49309	40.34	0.48
49322	39.36	0.49
49335	41.07	0.63
49345	40.53	0.63
49423	36.84	0.49
49429	36.84	0.59
49446	33.51	0.74
49643	29.56	0.65

Table 3e—Continued

MJD	Flux (Jy)	σ (Jy)
49661	29.69	0.84
49671	30.49	0.50
49678	29.96	0.65
49703	32.21	0.83
49713	30.44	0.38
49722	31.31	0.40
49736	31.17	0.55
49745	30.20	0.36
49753	29.58	0.63
49759	29.00	0.60
49814	27.42	0.42
49825	27.14	0.58
49831	27.30	0.66
49840	27.39	0.89

Table 3f.   37 GHz light curve for 3C 273 (Teräsranta, Tornikoski, Valtaoja).

MJD	Flux (Jy)	σ (Jy)
48308	36.88	0.58
48319	37.54	0.91
48343	39.71	0.41
48350	39.96	0.66
48367	41.10	0.39
48373	42.48	0.65
48389	44.07	0.67
48402	46.53	0.95
48413	47.27	0.60
48420	47.03	0.94
48437	46.23	0.77
48450	47.77	0.57
48457	49.33	0.89
48468	52.19	0.64
48473	51.80	1.08
48482	55.92	1.22
48493	55.70	0.62
48500	54.27	1.34
48555	49.64	0.77
48573	45.40	0.99
48581	44.83	1.03
48590	49.58	1.03
48607	45.78	0.94
48627	42.59	0.91
48642	42.05	0.51
48652	41.48	0.50
48665	41.00	0.86
48673	40.21	0.83
48722	37.57	0.53
48733	37.24	0.48
48741	37.44	0.65
48745	38.21	0.85
48777	36.42	0.38
48796	37.14	0.60

Table 3f—Continued

MJD	Flux (Jy)	σ (Jy)
48801	36.87	0.80
48817	36.60	0.49
48826	36.06	0.61
48868	35.56	0.52
48914	34.56	0.78
48924	33.45	0.44
48977	32.03	0.78
48985	31.76	0.38
48993	32.01	0.40
49026	28.95	0.40
49031	29.45	0.72
49043	27.23	0.52
49047	28.32	0.61
49057	27.73	0.43
49064	27.51	0.41
49096	26.64	0.46
49104	26.96	0.37
49112	27.13	0.55
49119	27.25	0.44
49129	28.78	0.43
49134	29.37	0.63
49164	28.45	0.36
49172	27.69	0.66
49201	29.29	0.38
49211	30.92	0.51
49216	30.85	0.75
49225	29.56	0.75
49288	32.59	0.55
49295	31.82	0.89
49306	31.98	0.60
49314	30.91	0.78
49329	32.21	0.66
49346	31.41	0.52
49360	32.21	0.77

Table 3f—Continued

MJD	Flux (Jy)	σ (Jy)
49385	30.29	0.80
49433	27.36	0.68
49445	26.16	0.42
49646	23.59	0.53
49664	25.22	1.17
49677	24.41	0.40
49712	24.83	0.51
49721	25.80	0.71
49734	24.92	0.55
49748	23.44	0.57
49758	23.30	0.30
49823	21.18	0.46
49832	20.47	0.55
49838	21.36	0.47

Table 4a.   0.45 mm fluxes of 3C 273 (McHardy).

MJD	Flux (Jy)	σ (Jy)
49137	5.70	1.00
49139	5.20	1.00
49140	6.80	1.00
49166	5.80	1.20
49214	3.60	1.00
49342	3.00	0.50
49344	3.90	1.00
49347	2.90	0.60
49409	3.80	0.60
49413	4.00	0.80

Table 4b.   0.8 mm fluxes of 3C 273 (McHardy).

MJD	Flux (Jy)	σ (Jy)
49118	12.20	1.50
49118	10.70	1.20
49119	8.80	1.70
49137	10.50	1.20
49139	11.70	1.20
49140	11.30	1.00
49161	8.20	0.60
49166	10.50	0.50
49214	9.70	0.70
49310	6.70	0.50
49311	7.00	0.50
49311	6.90	0.50
49312	6.90	0.50
49342	7.00	0.50
49343	7.10	0.50
49344	6.80	0.50
49347	6.90	0.40
49352	7.90	0.50
49353	7.00	0.50
49361	7.20	0.60
49409	7.70	0.50
49413	8.00	0.60
49422	9.00	0.50
49437	8.90	0.90
49450	8.30	0.60
49453	10.00	0.70
49465	7.80	0.50
49473	8.80	0.80

Table 4c.   1.1 mm fluxes of 3C 273 (McHardy).

MJD	Flux (Jy)	σ (Jy)
49118	14.20	1.00
49118	14.10	1.00
49119	14.50	0.90
49123	14.70	1.00
49137	14.00	0.80
49139	14.80	0.80
49140	14.10	0.70
49161	11.80	1.00
49166	14.40	0.90
49183	16.74	1.50
49187	14.60	0.50
49214	12.60	0.80
49310	9.80	0.40
49311	10.00	0.60
49311	9.70	0.50
49312	9.40	0.50
49314	10.20	0.60
49315	10.10	0.50
49316	10.50	0.50
49318	10.20	0.40
49319	10.20	0.50
49320	10.10	0.90
49326	9.90	0.60
49329	10.20	0.70
49342	9.40	0.50
49343	9.80	0.50
49344	9.60	0.50
49347	9.90	0.50
49348	10.10	0.60
49349	10.20	0.70
49350	10.40	0.70
49351	10.80	0.60
49352	10.50	0.60
49353	10.30	0.50

Table 4c—Continued

MJD	Flux (Jy)	σ (Jy)
49354	10.50	0.70
49355	10.50	0.50
49356	11.20	0.90
49357	11.30	0.80
49358	11.30	0.80
49359	11.30	0.70
49360	10.50	0.70
49361	10.30	0.60
49409	10.90	0.70
49413	10.50	0.70
49422	11.00	0.40
49437	10.80	0.80
49450	10.80	0.50
49453	12.10	0.70
49465	10.40	0.60
49472	10.10	0.60
49473	10.70	0.60
49474	10.70	0.60

Table 4d.   1.3 mm fluxes of 3C 273 (Tornikoski, Teräsranta, Valtaoja, Marscher, McHardy, Robson).

MJD	Flux (Jy)	σ (Jy)
48269	12.40	0.70
48300	17.60	1.10
48340	19.15	0.24
48341	18.13	0.10
48342	18.27	0.08
48351	22.26	1.60
48353	18.43	0.10
48353	18.47	0.09
48354	18.30	0.40
48354	18.51	0.06
48366	19.25	0.80
48393	17.96	0.90
48417	18.16	0.90
48441	13.38	1.03
48454	17.65	0.80
48480	20.60	1.20
48493	20.60	1.00
48514	19.60	1.00
48530	16.00	0.10
48533	15.10	0.10
48559	15.47	0.04
48571	14.53	0.19
48589	17.44	0.80
48607	16.90	0.07
48653	13.90	0.80
48654	12.60	1.00
48668	13.50	1.00
48697	14.60	0.90
48710	15.00	1.50
48714	13.60	1.20
48727	14.30	1.00
48749	13.50	0.40
48776	10.92	0.29
48777	11.49	0.48

Table 4d—Continued

MJD	Flux (Jy)	σ (Jy)
48858	12.50	0.88
49012	10.10	0.50
49025	13.70	0.70
49030	12.90	1.00
49031	13.20	1.40
49032	13.00	1.00
49044	14.32	0.57
49045	15.50	1.10
49046	15.27	0.58
49057	13.80	1.00
49082	16.90	0.50
49093	16.90	0.90
49094	16.00	0.90
49118	15.20	1.00
49118	16.20	1.00
49119	13.00	1.50
49137	15.20	0.80
49139	15.90	0.80
49140	15.40	0.80
49157	14.55	0.82
49166	14.90	0.80
49214	13.30	0.70
49312	11.50	0.80
49315	10.90	0.60
49322	12.18	0.41
49342	10.10	0.60
49343	10.30	0.50
49344	10.20	0.50
49347	10.40	0.60
49352	10.60	0.60
49353	10.80	0.50
49354	11.30	0.80
49360	11.10	0.80
49361	10.60	0.60

Table 4d—Continued

MJD	Flux (Jy)	σ (Jy)
49409	11.20	0.70
49413	12.30	0.90
49422	11.80	0.50
49453	13.10	0.80
49465	11.40	0.70
49472	10.30	0.60
49473	11.30	1.00
49474	11.00	0.90
49527	13.95	0.98
49527	13.99	0.98
49528	14.10	1.00
49528	14.97	1.05
49775	9.53	0.77
49775	10.37	0.83

Table 4e.   2.0 mm fluxes of 3C 273 (McHardy).

MJD	Flux (Jy)	σ (Jy)
49118	22.60	1.70
49118	20.90	1.50
49119	20.70	1.20
49137	19.60	1.00
49139	19.70	1.00
49140	20.20	1.00
49166	18.90	1.00
49214	18.20	0.50
49310	15.30	1.10
49311	15.70	1.10
49312	15.10	0.70
49314	15.70	1.00
49315	15.20	0.90
49316	15.00	0.80
49318	15.20	0.90
49319	15.20	0.90
49326	14.60	0.80
49329	15.70	1.20
49342	14.40	0.80
49343	14.30	0.80
49344	14.30	0.80
49347	14.40	0.90
49348	14.20	0.70
49349	14.60	1.00
49350	15.40	1.10
49351	15.30	1.00
49352	15.10	0.90
49353	15.20	0.80
49354	15.20	1.00
49355	15.10	0.80
49356	15.40	1.20
49357	15.70	1.10
49358	15.50	1.00
49359	15.10	0.90

Table 4e—Continued

MJD	Flux (Jy)	σ (Jy)
49360	15.20	1.00
49361	14.90	1.00
49409	14.00	0.80
49413	13.40	0.90
49422	15.10	0.70
49450	13.70	1.00
49453	17.00	1.00
49474	14.80	1.50

Table 4f.   3.0 mm fluxes of 3C 273 (Tornikoski, Teräsranta, Valtaoja).

MJD	Flux (Jy)	σ (Jy)
47896	16.96	0.69
47931	14.89	0.60
47937	15.61	0.63
47951	15.78	0.63
47966	14.53	0.58
47981	12.84	0.52
47988	13.26	0.53
47989	13.47	0.54
47994	14.11	0.57
47995	13.94	0.56
47996	13.85	0.56
47997	14.27	0.57
47998	14.44	0.58
48004	14.23	0.57
48011	15.26	0.61
48022	17.76	0.71
48053	28.11	1.14
48062	29.61	1.19
48071	32.38	1.30
48104	33.49	1.35
48231	29.17	1.17
48256	25.31	1.08
48314	32.23	1.29
48351	36.22	1.46
48430	33.86	1.36
48455	34.93	1.40
48469	36.10	1.50
48591	29.98	1.20
48592	29.70	1.19
48614	27.13	1.09
48615	26.61	1.07
48664	29.47	1.19
48665	28.03	1.12
48726	28.10	1.13

Table 4f—Continued

MJD	Flux (Jy)	σ (Jy)
48785	25.38	1.02
48857	25.21	1.01
48987	18.28	0.75
49043	21.80	0.88
49078	26.30	1.05
49139	28.57	1.14
49155	23.43	0.94
49323	23.13	0.93
49326	22.51	0.90
49326	23.64	0.95
49350	23.37	0.94
49384	20.70	0.83
49384	22.41	0.90
49385	20.62	0.83
49385	23.15	0.93
49466	19.91	0.81
49467	20.14	0.81
49504	20.25	0.82
49528	21.97	0.88
49565	21.38	0.86
49698	22.03	0.89
49699	21.01	0.96
49749	18.10	0.73
49776	16.50	0.66
49776	16.94	0.68

Table 5. Summary of IR and optical observations of 3C 273 (Courvoisier, Marscher, Robson, Wagner).

	U		B		V		R		I		J		H		
MJD	Flux (mJy)	σ (mJy)	Flux (mJy)	σ (mJy)	Flux (mJy)	σ (mJy)	Flux (mJy)	σ (mJy)	Flux (mJy)	σ (mJy)	Flux (mJy)	σ (mJy)	Flux (mJy)	σ (mJy)	Flux (mJy)
49078	$\cdots$	$\cdots$	30.34	1.37	30.76	1.38	29.24	1.32	34.51	1.55	$\cdots$	$\cdots$	$\cdots$	$\cdots$	$\cdots$
49304	$\cdots$	$\cdots$	$\cdots$	$\cdots$	$\cdots$	$\cdots$	26.67	0.49	$\cdots$	$\cdots$	$\cdots$	$\cdots$	$\cdots$	$\cdots$	$\cdots$
49310	$\cdots$	$\cdots$	$\cdots$	$\cdots$	$\cdots$	$\cdots$	26.92	0.49	$\cdots$	$\cdots$	$\cdots$	$\cdots$	$\cdots$	$\cdots$	$\cdots$
49330	$\cdots$	$\cdots$	$\cdots$	$\cdots$	$\cdots$	$\cdots$	$\cdots$	$\cdots$	$\cdots$	$\cdots$	38.02	1.71	50.82	2.29	84.33
49331	$\cdots$	$\cdots$	$\cdots$	$\cdots$	$\cdots$	$\cdots$	$\cdots$	$\cdots$	$\cdots$	$\cdots$	41.30	1.86	52.24	2.35	88.31
49372	$\cdots$	$\cdots$	30.62	1.38	31.05	1.40	29.24	1.32	26.92	1.21	$\cdots$	$\cdots$	$\cdots$	$\cdots$	$\cdots$
49386	31.14	0.28	30.37	0.20	33.18	0.19	$\cdots$	$\cdots$	$\cdots$	$\cdots$	$\cdots$	$\cdots$	$\cdots$	$\cdots$	$\cdots$
49398	$\cdots$	$\cdots$	$\cdots$	$\cdots$	$\cdots$	$\cdots$	27.42	0.50	$\cdots$	$\cdots$	$\cdots$	$\cdots$	$\cdots$	$\cdots$	$\cdots$
49399	31.98	0.28	31.48	0.20	33.89	0.19	$\cdots$	$\cdots$	$\cdots$	$\cdots$	$\cdots$	$\cdots$	$\cdots$	$\cdots$	$\cdots$
49400	32.42	0.28	31.66	0.20	33.64	0.19	27.67	0.51	$\cdots$	$\cdots$	$\cdots$	$\cdots$	$\cdots$	$\cdots$	$\cdots$
49414	33.12	0.28	32.10	0.20	34.65	0.19	$\cdots$	$\cdots$	$\cdots$	$\cdots$	$\cdots$	$\cdots$	$\cdots$	$\cdots$	$\cdots$

Table 6. Summary of IUE/EUVE observations of 3C 273 (Kafatos). UV-fluxes are corrected for interstellar absorption using a value for E(B-V) = 0.03 and the reddening law of Seaton (1979).

MJD	LWP($1.07 \cdot 10^{15}$ Hz)		SWP($2.14 \cdot 10^{15}$ Hz)		DSS($2.99 \cdot 10^{16}$ Hz)	
	Flux (mJy)	σ (mJy)	Flux (mJy)	σ (mJy)	Flux (mJy)	σ (mJy)
49360	26.30	0.99	13.93	0.48	$\cdots$	$\cdots$
49523	27.56	0.99	16.36	0.48	$\cdots$	$\cdots$
49360-49366	$\cdots$	$\cdots$	$\cdots$	$\cdots$	0.319	0.064
49720-49729	24.84	0.76	13.46	0.36	0.195	0.039

Table 7.   ASCA spectra and fluxes of 3C 273 in December 1993 (Makino, Kii).

Date (MJD)	Focal Plane Instruments	mean frequency (10^{18}Hz)	Flux density (μJy)	Flux (2-10 keV) (10^{-10}erg/cm^{2}s)	Photon Indices (90% error area)
Dec 16	SIS-S0	1.058	9.84	1.72	1.60 (1.59-1.62)
(49337)	SIS-S1	1.056	9.51	1.66	1.61 (1.59-1.62)
	GIS-S2	1.061	9.30	1.63	1.59 (1.57-1.60)
	GIS-S3	1.058	9.26	1.62	1.60 (1.58-1.61)
Dec 19	SIS-S0	1.065	8.63	1.52	1.57 (1.56-1.58)
(49340)	SIS-S1	1.061	8.39	1.47	1.59 (1.58-1.60)
	GIS-S2	1.067	7.59	1.34	1.56 (1.55-1.58)
	GIS-S3	1.067	7.70	1.36	1.56 (1.55-1.57)
Dec 20	SIS-S0	1.058	8.12	1.42	1.60 (1.59-1.62)
(49341)	SIS-S1	1.061	7.93	1.39	1.59 (1.57-1.61)
	GIS-S2	1.061	7.19	1.26	1.59 (1.57-1.61)
	GIS-S3	1.063	7.17	1.26	1.58 (1.56-1.59)
Dec 23	SIS-S0	1.065	8.40	1.48	1.57 (1.56-1.59)
(49344)	SIS-S1	1.067	8.33	1.47	1.56 (1.55-1.58)
	GIS-S2	1.069	7.57	1.34	1.55 (1.53-1.57)
	GIS-S3	1.069	7.57	1.34	1.55 (1.53-1.56)
Dec 27	SIS-S0	1.074	10.30	1.83	1.53 (1.52-1.55)
(49348)	SIS-S1	1.079	10.42	1.86	1.51 (1.49-1.52)
	GIS-S2	1.081	9.17	1.64	1.50 (1.49-1.52)
	GIS-S3	1.079	9.19	1.64	1.51 (1.49-1.53)

Table 8.   OSSE spectrum of 3C 273
during MJD 49341-49348 (Johnson).

mean frequency (Hz)	Flux (μJy)	σ (μJy)
$2.1 \cdot 10^{19}$	1.40	0.14
$5.1 \cdot 10^{19}$	0.76	0.16
$1.2 \cdot 10^{20}$	0.13	0.19
$2.6 \cdot 10^{20}$	0.48	0.35
$5.9 \cdot 10^{20}$	0.00	0.22
$1.5 \cdot 10^{21}$	0.11	0.10

Table 9.   COMPTEL spectrum of
3C 273 during MJD 49279-49355
(Collmar).

mean frequency (Hz)	Flux (μJy)	σ (μJy)
$2.1 \cdot 10^{20}$	0.12	0.077
$4.0 \cdot 10^{20}$	0.097	0.023
$1.2 \cdot 10^{21}$	0.036	0.0082
$4.0 \cdot 10^{21}$	< 0.0078	